Three-dimensional elastohydrodynamics of a thin plate oscillating above a wall

R. J. Clarke*
Department of Engineering Science, University of Auckland, Auckland, New Zealand

O. E. Jensen and J. Billingham
School of Mathematical Sciences, University of Nottingham, University Park, Nottingham, NG7 2RD, United Kingdom

(Received 12 May 2008; published 26 November 2008)

We consider deflections of a thin rectangular elastic plate that is submerged within a Newtonian fluid. The plate is clamped along one edge and supported horizontally over a plane horizontal wall. We consider both external driving, where the clamped edge is vibrated vertically at high frequencies, and thermal driving, where the plate fluctuates under Brownian motion. In both cases, the amplitude of oscillation is assumed sufficiently small that the resulting flow has little convective inertia, although the oscillation frequency is sufficiently high to generate substantial unsteady inertia in the flow, a common scenario in many nano- and microdevices. We exploit the plate's thinness to develop an integral-equation representation for the three-dimensional flow (a so-called thin-plate theory) which offers considerable computational savings over a full boundary-integral formulation. Limiting cases of high oscillation frequencies and small wall-plate separation distances are studied separately, leading to further simplified descriptions for the hydrodynamics. We validate these reduced integral representations against full boundary-integral computations, and identify the parameter ranges over which these simplified formulations are valid. Addressing the full flow-structure interaction, we also examine the limits of simpler two-dimensional hydrodynamic models. We compare the responses of a narrow plate under two- and three-dimensional hydrodynamic loading, and report differences in the frequency response curves that occur when the plate operates in water, in contrast to the excellent agreement observed in air.

DOI: 10.1103/PhysRevE.78.056310 PACS number(s): 47.61.Fg, 07.10.Cm, 07.79.Lh

I. INTRODUCTION

Understanding the way in which fluid damping can influence the response of a microscopic flexible plate to external and thermal driving provides important insights into the functioning of a host of microdevices. Although plate dimensions and deflection amplitudes within such devices are often sufficiently small that convective inertia in the flow can be neglected, the high speeds reached by many microdevice components often result in highly unsteady flows. Advances in microtechnologies are therefore driving an urgent need to understand better these unsteady low-Reynolds-number flows, which have been studied since the early work by Stokes [1] on the two-dimensional flow driven by an oscillating, infinite-length circular cylinder.

Some of the most advanced elastohydrodynamical modeling has been conducted with the atomic-force microscope (AFM) in mind, where the forced oscillations of a narrow microcantilever are used to map the surface topology of a biological specimen within a fluid environment [2]. Important contributions in this respect have been made by coupling classical results for two-dimensional flow around the cantilever to a one-dimensional Euler-Bernoulli beam description for the elastic behavior [3–5]. Other examples include single-molecule biosensors, which measure the response of a nanocantilever as molecules bind to it [6], as well as an increasing assortment of microelectromechanical systems.

In general, however, microdevices contain plates that are finite in length and can bend significantly across their width (in full-contact-mode atomic-force microscopy, for example, spanwise deflections are used to determine specimen surface properties; see [7]). In the absence of hydrodynamic effects, a number of workers [8–10] have computed the elastic response of finite-width plates with realistic AFM cantilever shapes. More recent work on the hydrodynamical aspects has used slender-body theory to examine the three-dimensional fluid effects near the ends of a finite-length cantilever that has negligible width [11].

The precise details of a flow within and around a microdevice will, of course, depend upon the exact configuration of the device in question, which will vary considerably across different technologies. The AFM cantilever, for instance, is often attached to the end of a thin chip (often alongside several other cantilevers), whereas other microdevices may have their elastic plates embedded into solid vertical surfaces. It is not our intention here to faithfully reproduce the configuration of any one specific microdevice, but rather to develop useful computational techniques and to illustrate the potential limitations of certain modeling assumptions, which we hope will find broad application.

Here we present a study of the coupled fluid-solid behavior of an elastic rectangular plate that is clamped at one end (although details of the support structure are omitted) and submerged within a Newtonian fluid. This plate oscillates at high frequencies but with low amplitudes, above a plane wall. This is achieved by deriving an integral formulation for the oscillatory Stokes flow around a thin three-dimensional body (so-called thin-plate theory) that offers considerable computational savings over a full three-dimensional boundary-integral method. On a standard desktop PC, and in the purely hydrodynamic regime where the plate is assumed rigid, thin-plate theory requires just 1% of the computational

*rj.clarke@auckland.ac.nz

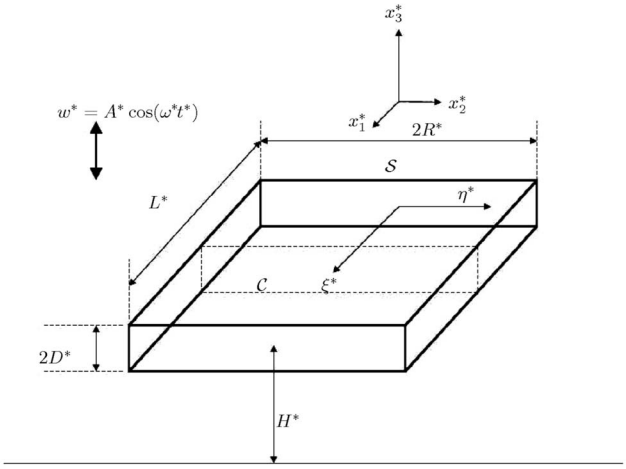

FIG. 1. An elastic plate of length L^*, width $2R^*$, and thickness $2D^*$ oscillates with frequency ω^* and amplitude A^* normal to a plane wall ($x_3^*=0$). The plate's plane of vertical symmetry, parametrized by (ξ^*, η^*), lies a distance H^* from the wall. The undeflected plate surface is denoted $\mathcal{S}$ and $\mathcal{C}$ is the perimeter of the plate's cross section in the x_2^*-x_3^* plane.

time needed by a full boundary-integral formulation. When the plate is nonrigid, thin-plate theory allows computations to be made on a conventional desktop PC, which would otherwise be prohibitively expensive using boundary-integral methods.

The limiting case of a rigid plate is studied initially, in order to validate our simplified flow formulation and extend earlier work on wall effects in two-dimensional oscillatory Stokes flow [12] into three dimensions. This is followed by a general treatment of the elastohydrodynamics, which allows us to predict the frequency response of an externally or thermally driven, fluid-damped elastic plate. We identify occasions when the flow in such models may be considered to be essentially two dimensional and, importantly, occasions where a three-dimensional flow model may be necessary.

We begin in Sec. II by introducing the elastic-plate equations governing the solid body (Sec. II A) and the unsteady Stokes equations governing the flow (Sec. II B) and then describe how these couple together. Circumstances under which simplifications to the model can be made are identified in Sec. III. We describe the numerical approach in Sec. IV, and results are then presented in Sec. V. Overall conclusions for the work are summarized in Sec. VI.

II. FORMULATION

We consider a thin elastic rectangular plate of length L^*, width $2R^*$, and uniform thickness $2D^*$ ($2D^* \ll R^*, L^*$) immersed in a Newtonian fluid of density ρ and kinematic viscosity ν. The plate's plane of vertical symmetry (parametrized by coordinates ξ^* and η^*) lies at a distance H^* above a horizontal wall; the wall is located at $x_3^*=0$ with respect to Cartesian coordinates (x_1^*, x_2^*, x_3^*) (see Fig. 1). The plate has uniform density ρ_p, Young's modulus E [$O(10^{12}$ g cm^{-1} s^{-2}) for a silicon nitride AFM cantilever, or equivalently O (100 GPa)], Poisson ratio ν_p (the ratio of transverse over compressive strain, which is approximately 0.3 for AFM cantilevers), and hence a flexural rigidity $\mathcal{D}=E(2D)^{*3}/12(1-\nu_p^2)$. The plate oscillates in a vertical direction with frequency ω^* and amplitude $A^* \ll 2D^*$, causing vertical deflections $W^*(\xi^*, \eta^*, t^*)$ of the plate's plane of vertical symmetry. Although in most applications torsional motions (i.e., motions in the x_2^*-x_3^* plane) of the plate will be subdominant, and of less interest than the vertical displacements, such twisting behavior is decoupled from motions in the x_3^* direction, due to the linearity of the governing equations, and can be included through straightforward modifications to the model (although we do not do so in this study, but see [13]).

In what follows we scale lengths on L^*, oscillation frequency ω^* on the natural frequency $\omega_0 \equiv \sqrt{\mathcal{D}/\rho_p(2D^*)(L^*)^4}$, time t^* on ω_0^{-1}, deflections on A^*, flow speeds U^* on $A^*\omega^*$, and pressure on $\rho\nu U^*/L^*$ and take $\Delta \equiv (H^*-D^*)/L^*$ to be the dimensionless separation distance between the bottom of the plate and the wall. The nondimensional plate width and thickness are then denoted by $2R$ and $2D$, respectively. The fluid loading per unit area F^* is scaled on $A^*\omega^*\mu/L^*$.

A. Solid-body dynamics

Expressing strains in terms of plate curvature and assuming a Hookean stress-strain relationship, a vertical force balance and moment equilibria lead to the dimensional linear plate equation [14]

$$\mathcal{D}\nabla^{*4}W^* + \rho_p(2D^*)\frac{\partial^2 W^*}{\partial t^{*2}} = F^* \tag{1}$$

($\nabla^{*2} \equiv \partial^2/\partial\xi^{*2} + \partial^2/\partial\eta^{*2}$) which is applicable here due to the small nature of the deformation amplitudes. Looking for oscillatory solutions $W^*(\xi^*, \eta^*, t^*) = \mathrm{Re}[A^* w(\xi^*, \eta^*) e^{i\omega^* t^*}]$ under the above nondimensionalization, Eq. (1) becomes

$$\nabla^4 w - \omega^2 w = M\Omega F, \tag{2}$$

where $M \equiv \nu/\omega_0(L^*)^2$ and $\Omega = \rho L^*/\rho_p(2D^*)$ (see Table I in Sec. V B below for typical operating values of Ω and M in both air and water).

Driving the plate externally involves prescribing the following boundary conditions at $\xi=0$:

$$w(0,\eta) = 1, \quad \frac{\partial w}{\partial \xi}(0,\eta) = 0 \quad \text{for } -R \leqslant \eta \leqslant R; \tag{3a}$$

and invoking free-edge conditions along the other sides [see Eq. (12) for a justification as to why hydrodynamic stresses on these sides can be neglected when the plate is thin]

$$\frac{\partial^2 w}{\partial \xi^2} + \nu_p \frac{\partial^2 w}{\partial \eta^2} = \frac{\partial^3 w}{\partial \xi^3} + (2-\nu_p)\frac{\partial^3 w}{\partial \xi \partial \eta^2} = 0$$

$$\text{on } \xi = 1, \ -R \leqslant \eta \leqslant R, \tag{3b}$$

$$\frac{\partial^2 w}{\partial \eta^2} + \nu_p \frac{\partial^2 w}{\partial \xi^2} = \frac{\partial^3 w}{\partial \eta^3} + (2-\nu_p)\frac{\partial^3 w}{\partial \xi^2 \partial \eta} = 0$$

$$\text{on } \eta = \pm R, \ 0 \leqslant \xi \leqslant 1. \tag{3c}$$

The behavior under thermal driving, however, is determined by computing the response of the plate following the application of a point torque to the plate tip, in accordance with the fluctuation-dissipation theorem approach [5,6]. Under these circumstances the boundary conditions become

$$w = 0, \quad \frac{\partial w}{\partial \xi} = 0 \quad \text{on } \xi = 0, \ -R \leqslant \eta \leqslant R, \tag{4a}$$

$$\frac{\partial^2 w}{\partial \xi^2} + \nu_p \frac{\partial^2 w}{\partial \eta^2} = 1 \quad \text{on } \xi = 1, \ -R \leqslant \eta \leqslant R, \tag{4b}$$

$$\frac{\partial^3 w}{\partial \xi^3} + (2 - \nu_p) \frac{\partial^3 w}{\partial \xi \partial \eta^2} = 0 \quad \text{on } \xi = 1, \ -R \leqslant \eta \leqslant R, \tag{4c}$$

$$\frac{\partial^2 w}{\partial \eta^2} + \nu_p \frac{\partial^2 w}{\partial \xi^2} = \frac{\partial^3 w}{\partial \eta^3} + (2 - \nu_p) \frac{\partial^3 w}{\partial \xi^2 \partial \eta} = 0 \quad \text{on } \eta = \pm R, \ 0 \leqslant \xi \leqslant 1. \tag{4d}$$

For computational purposes we decompose the fourth-order equation (2) into a pair of coupled second-order equations

$$\nabla^2 v - \omega^2 w = M \Omega F, \tag{5a}$$

$$v = \nabla^2 w \tag{5b}$$

(where $-v$ is the average curvature, which can be shown to be invariant under rotations of the coordinate system in the x_1-x_2 plane [14]) with the externally driven boundary conditions along the non clamped edges (3b) and (3c) now becoming

$$\nu_p v + (1 - \nu_p) \frac{\partial^2 w}{\partial \xi^2} = (2 - \nu_p) \frac{\partial v}{\partial \xi} + (\nu_p - 1) \frac{\partial^3 w}{\partial \xi^3} = 0 \quad \text{on } \xi = 1, \ -R \leqslant \eta \leqslant R, \tag{6a}$$

$$\nu_p v + (1 - \nu_p) \frac{\partial^2 w}{\partial \eta^2} = (2 - \nu_p) \frac{\partial v}{\partial \eta} + (\nu_p - 1) \frac{\partial^3 w}{\partial \eta^3} = 0 \quad \text{on } \eta = \pm R, \ 0 \leqslant \xi \leqslant 1, \tag{6b}$$

whereas the thermal boundary conditions along the non-clamped edges [Eqs. (4b)–(4d)] become

$$\nu_p v + (1 - \nu_p) \frac{\partial^2 w}{\partial \xi^2} = 1 \quad \text{on } \xi = 1, \ -R \leqslant \eta \leqslant R, \tag{7a}$$

$$(2 - \nu_p) \frac{\partial v}{\partial \xi} + (\nu_p - 1) \frac{\partial^3 w}{\partial \xi^3} = 0 \quad \text{on } \xi = 1, \ -R \leqslant \eta \leqslant R, \tag{7b}$$

$$\nu_p v + (1 - \nu_p) \frac{\partial^2 w}{\partial \eta^2} = (2 - \nu_p) \frac{\partial v}{\partial \eta} + (\nu_p - 1) \frac{\partial^3 w}{\partial \eta^3} = 0 \quad \text{on } \eta = \pm R, \ 0 \leqslant \xi \leqslant 1. \tag{7c}$$

In general, the hydrodynamic loading F will be a functional of the deflection w. The assumption of small-amplitude deflections, however, considerably simplifies the nature of the elastohydrodynamic coupling.

B. Flow dynamics

The amplitude constraint $A^* \ll 2D^*$ allows us to consider low-Reynolds-number unsteady flow and to linearize the boundary conditions. Hence, for hydrodynamical purposes, we need only consider the rigid plate surface $\mathcal{S}$ (as depicted in Fig. 1). We look for flows of the form $\mathrm{Re}(U^* \boldsymbol{u} e^{i\omega^* t^*})$ which, under nondimensionalization, are governed by the oscillatory Stokes equations [15]

$$i\gamma^2 \boldsymbol{u} = -\boldsymbol{\nabla} p + \nabla^2 \boldsymbol{u}, \quad \boldsymbol{\nabla} \cdot \boldsymbol{u} = 0, \tag{8}$$

where $\boldsymbol{u}$ and p are the fluid velocity and pressure, respectively, and $\gamma \equiv L^* \sqrt{\omega^* / \nu} = M^{-1/2} \omega^{1/2}$. Equations (8) must be solved subject to the boundary conditions

$$\boldsymbol{u}|_{\mathcal{S}} = i\omega w(\xi, \eta) \hat{\boldsymbol{x}}_3, \quad \boldsymbol{u}(x_1, x_2, 0) = \boldsymbol{0},$$

$$\boldsymbol{u} \to \boldsymbol{0} \text{ as } |\boldsymbol{x}| \to \infty \text{ for } x_3 \geqslant 0, \tag{9}$$

where $\hat{\boldsymbol{x}}_3$ is the unit normal in the x_3 direction, i.e., the velocity at a point on the plate's surface is proportional to the deflection of its midplane at the location (ξ, η), the vertical projection of the surface point onto the midplane. However, a note of caution is in order. In the case of extremely small gap thicknesses or in the presence of rarified gases, the above boundary conditions may need to be modified to take account of failings in the no-slip condition in these regimes [12,16].

The fluid loading on the plate F is given by

$$F(\xi, \eta; \gamma, \Delta) = \hat{\boldsymbol{n}} \cdot \boldsymbol{\sigma} \cdot \hat{\boldsymbol{n}}|_{\mathcal{S}} = \hat{\boldsymbol{n}} \cdot (-p\boldsymbol{I} + \boldsymbol{\nabla u} + \boldsymbol{\nabla u}^T) \cdot \hat{\boldsymbol{n}}|_{\mathcal{S}}, \tag{10}$$

where $\boldsymbol{\sigma}$ is the Newtonian stress tensor for the fluid.

Oscillatory Stokes flow can be expressed in boundary-integral form as [17]

$$u_i(\boldsymbol{Y}) = \frac{1}{8\pi} \int_{\mathcal{S}} g_j(\boldsymbol{y}) \bar{S}_{ij}(\boldsymbol{y}, \boldsymbol{Y}; \gamma, \Delta) d\mathcal{A},$$

$$g_j(\boldsymbol{y}) = \sigma_{jk} \hat{n}_k - i\gamma^2 u_k y_k \hat{n}_j \tag{11}$$

(summing over repeated subscripts $1 \leqslant i, j, k \leqslant 3$) where $\boldsymbol{y} \in \mathcal{S}$ and $\boldsymbol{Y}$ is, in general, any point in the fluid domain. By allowing $\boldsymbol{Y} \in \mathcal{S}$, where the flow velocity is known via the boundary conditions, we obtain an integral equation for the unknown function $\boldsymbol{g}$. $\bar{S}_{ij}$ is the symmetrical oscillatory Stokeslet which accounts for the presence of a plane wall, as derived by Pozrikidis [18] (see Appendix A). Since

$$\begin{aligned} g_3|_{\mathcal{S}_U} + g_3|_{\mathcal{S}_L} &= (\sigma_{3k} \hat{n}_k - i\gamma^2 (iw) y_3 \hat{n}_3)|_{\mathcal{S}_U} + (\sigma_{3k} \hat{n}_k - i\gamma^2 (iw) y_3 \hat{n}_3)|_{\mathcal{S}_L} \\ &= \sigma_{3k} \hat{n}_k|_{\mathcal{S}_U} + \sigma_{3k} \hat{n}_k|_{\mathcal{S}_L} + \gamma^2 w[(\Delta + 2D) - \Delta] \\ &= F + 2D\gamma^2 w, \end{aligned} \tag{12}$$

determining the additive contribution to g_3 from the upper

($\mathcal{S}_U$) and lower ($\mathcal{S}_L$) horizontal surfaces of the plate provides the hydrodynamic loading on these surfaces up to a known constant $2D\gamma^2 w \ll \gamma^2$. This known constant is negligible when $\gamma \lesssim O(1)$ since $2D \ll R \lesssim 1$ and is subdominant to the $O(\gamma^2)$ contributions from $F \equiv \sigma_{3k}\hat{n}_k|_{\mathcal{S}_U} + \sigma_{3k}\hat{n}_k|_{\mathcal{S}_L}$ (specifically the added mass) when $\gamma \gg 1$, and hence can be neglected.

This additive contribution of stresses on the horizontal surfaces can be approximated by exploiting the thinness of the plate ($D \ll R$) to expand the surface distribution of Stokeslets in Eq. (11) about the midplane of the plate at $x_3 = \Delta + D$. This allows us to approximate the flow using just a single plane of three-dimensional image Stokeslets over the plate's midplane (rather than a full surface covering) as

$$u_i(\Lambda, \Xi) = \frac{1}{8\pi}\int_{-R}^{R}\int_{0}^{1} \bar{S}_{ij}(\boldsymbol{x}, \boldsymbol{X}; \gamma, \Delta) f_j(\xi, \eta) d\xi\, d\eta, \quad (13)$$

where $\boldsymbol{x} = \xi\hat{\boldsymbol{x}}_1 + \eta\hat{\boldsymbol{x}}_2 + (\Delta + D)\hat{\boldsymbol{x}}_3$ is a point in the midplane and $\boldsymbol{X} = \Lambda\hat{\boldsymbol{x}}_1 + \Xi\hat{\boldsymbol{x}}_2 + (\Delta + 2D)\hat{\boldsymbol{x}}_3$ is a point on the upper surface. Therefore, from the above discussion, we expect $f_3 = g_3|_{\mathcal{S}_U} + g_3|_{\mathcal{S}_L} + O(D\gamma^2)$.

We note from Appendix A that many of the terms involving $\boldsymbol{y}$ and $\boldsymbol{Y}$ contained within $\bar{S}_{ij}$ in Eq. (11) are premultiplied by γ. Therefore, to expand about the midplane, we require $\gamma D \ll 1$. In other words, the γ^{-1} distances over which vorticity diffuses during each oscillation should be much greater than the plate's thickness $2D$ for the present approximation to be valid.

Consequently, the flows around the $2D$-thick edges of the plate are quasisteady and dominated by $O(s'^{-\beta_0})$ singularities where horizontal and vertical surfaces join [19]. The variable s' here is a measure of the distance along the edge to the nearest corner and $\beta_0 \approx 0.5$. The drag contribution from the sides is therefore $O(D^{-\beta_0+1}) = o(1)$ and hence can be neglected.

We shall refer to Eq. (13) as the three-dimensional thin-plate theory (3D TPT) approximation. It is anticipated that f_3 will provide the additive hydrodynamic stresses from the upper and lower surfaces, and hence the dominant hydrodynamic loading on the plate. Therefore, Eq. (13) presents a more efficient and appealing method for computing hydrodynamic damping than the full three-dimensional boundary-integral treatment Eq. (11). Furthermore, since the linear elasticity equations are derived in the asymptotic limit of zero thickness, 3D TPT is the consistent formulation for the hydrodynamic loading.

Under certain circumstances, namely, at high frequencies of oscillation or small plate-wall separation distances, we are able to simplify the flow formulation still further, in ways that we discuss in Sec. III.

III. LIMITING CASES: REDUCTION OF DIMENSIONALITY VIA SCREENING EFFECTS

In general, the flows generated by an oscillating plate will be three dimensional due to the generation of flows around the edges of the plate. Sufficiently close to the edges these flows will be quasisteady in nature, although for oscillatory flows it is well known that the range of viscous effects scale with the inverse of the oscillation frequency (for example, see [20,21]). Hence, at high frequencies three-dimensional viscous effects are confined to thin $O(\gamma^{-1})$ Stokes layers about the edges, and the flow outside of these layers is largely inviscid. However, since these inviscid flows are confined to distances comparable with the relevant characteristic length scale, the three-dimensional edge flows generated by short edges have limited range. This screening of three-dimensional flows at large frequencies was observed with slender oscillating rods [11], where three-dimensional viscous and invisicd flows generated at the ends of the rod were limited to $O(\gamma^{-1})$ and $O(R_0)$ distances, respectively (where $R_0 \ll 1$ is the ratio of the rod's radius to its length). For the case of a plate, we therefore expect frequency screening to occur when $\max(R, \gamma^{-1}) \ll \min(1, \Delta)$. Decreasing the wall separation distance provides a second mechanism for screening three-dimensional flow effects [11], and occurs when $\Delta \ll \min(1, R)$. We now consider these two limits in turn.

A. Hydrodynamic frequency screening [$\max(R, \gamma^{-1}) \ll \min(1, \Delta)$]

When the plate is much longer than it is wide ($D \ll R \ll 1$) and the range over which vorticity can diffuse is small with respect to plate length ($\gamma^{-1} \ll 1$), we expect three-dimensionality in the flow to be confined to the plate ends ($\xi = 0, 1$) even in the effective absence of a wall ($\gamma^{-1} \ll \Delta$, i.e., when the separation distance is much greater than the thickness of the Stokes layers present on both the wall and plate surface).

The locally two-dimensional flow along the length of the plate can also be described through a boundary-integral formulation analogous to (11) that uses a midplane distribution of two-dimensional oscillatory Stokeslets $\bar{S}'_{ij}$ which take account of the wall's presence (as computed by Chu and Kim [22]; see Appendix B). In this limit it proves useful to rescale lengths on the plate width rather than plate length, $\boldsymbol{x}' \equiv \boldsymbol{x}/R$, and to rescale the frequency parameter in a similar manner with $\gamma' \equiv R\gamma$. The two-dimensional boundary-integral representation for the flow then becomes [23]

$$u'_i(\boldsymbol{Y}') = \frac{1}{4\pi}\int_{\mathcal{C}} g'_j(\boldsymbol{y}')\bar{S}'_{ij}(\boldsymbol{y}', \boldsymbol{Y}'; \gamma', \Delta') d\mathcal{A},$$

$$g'_j(\boldsymbol{y}') = \sigma'_{jk}\hat{n}_k - i\gamma'^2 u'_k y'_k \hat{n}_j \quad (14)$$

(summing over repeated subscripts $1 \leq i, j, k \leq 2$) where $\boldsymbol{y}' \in \mathcal{C}$ (the perimeter of the plate's length), $\boldsymbol{u}'$ refers to the flow in the local (x'_2, x'_3) plane, $\boldsymbol{Y}'$ is a point in this same plane (but not within the body of the plate), and $\boldsymbol{\sigma}'$ represents the corresponding stress tensor for the two-dimensional flow. As in the three-dimensional case, we expect the overall hydrodynamic load on the two-dimensional plate F' to be dominated by the fluid stresses on the upper and lower surfaces,

$$F' = \sigma'_{2k}\hat{n}_k|_{\mathcal{C}_U} + \sigma'_{2k}\hat{n}_k|_{\mathcal{C}_L}, \quad (15)$$

where $\mathcal{C}_U$ and $\mathcal{C}_L$ denote the upper and lower surfaces of $\mathcal{C}$, respectively.

As before, when the thickness of a two-dimensional plate is small compared with its other dimensions, we can expand the surface distribution of Stokeslets in the boundary-integral expression about the plate's midplane ($x_3'=\Delta'+D'$), leading to a two-dimensional TPT approximation

$$u_i'(\eta') = -\frac{1}{4\pi}\int_{-1}^{1} \bar{S}_{ij}'(\boldsymbol{x}',\boldsymbol{X}';\gamma',\Delta')f_j'(\Xi')d\Xi', \quad (16)$$

where $\boldsymbol{f}'$ denotes a distribution of two-dimensional Stokeslets which, as in the three-dimensional case, is expected to approximate F' accurately, from which the overall load on the plate can be computed. Here, $\boldsymbol{x}'=\Xi'\hat{\boldsymbol{x}}_2+(\Delta'+D')\hat{\boldsymbol{x}}_3$ is a point in the midplane in the (x_2,x_3) plane and $\boldsymbol{X}'=\eta'\hat{x}_2+(\Delta'+2D')\hat{\boldsymbol{x}}_3$ is a point on the upper surface.

Unlike the slender-body-flow approximation for flow around a body with rodlike geometry [11], in general no leading-order local force–velocity relationship exists in the 2D TPT formulation (16) upon which an asymptotic expansion can be constructed. However, when the frequency of oscillation is high ($\gamma' \gg 1$) viscous effects become localized, which can lead to significant simplifications. This can be seen by splitting the two-dimensional oscillatory free-space Stokeslet S_{ij}' (see Appendix B) into its inviscid and viscous contributions,

$$\begin{aligned} u_i'(\eta') &= \frac{1}{4\pi}\int_{-1}^{1} S_{ij}'(\hat{\boldsymbol{x}}';\gamma')f_j'(\Xi')d\Xi' \\ &= \frac{1}{2\pi(\lambda')^2}\int_{-1}^{1} Q_{ij}(\hat{\boldsymbol{x}}')f_j'(\Xi')d\Xi' \\ &\quad - \frac{1}{2\pi}\int_{-1}^{1}\left[K_0(\lambda'\hat{r}')\left(\delta_{ij}+\frac{\hat{x}_i'\hat{x}_j'}{\hat{r}'^2}\right)\right. \\ &\quad \left. - \frac{K_1(\lambda'\hat{r}')}{\hat{r}'}\left(\delta_{ij}-\frac{2\hat{x}_i'\hat{x}_j'}{\hat{r}'^2}\right)\right]f_j'(\Xi')d\Xi', \quad (17) \end{aligned}$$

where $\hat{\boldsymbol{x}}'=\boldsymbol{x}'-\boldsymbol{X}'$, $r'=|\hat{\boldsymbol{x}}'|$, and $\lambda'=\sqrt{i}\gamma'$. The second integral contains viscous terms, while the first integral contains a distribution of two-dimensional dipoles

$$Q_{ij} \equiv \frac{\delta_{ij}}{\hat{r}'^2} - \frac{2\hat{x}_i'\hat{x}_j'}{\hat{r}'^4}. \quad (18)$$

The modified Bessel functions $K_0(z)$ and $K_1(z)$ in the viscous expression exhibit exponential decay for $|z| \gg 1$ and so we expect a non-negligible viscous contribution to the second integral over only an $O(\gamma^{-1})$ interval about $\Xi'=\eta'$. This suggests the rescaling $\Xi'=\eta'+(\gamma'^{-1})\Xi''$, in which case

$$\begin{aligned} u_i'(\eta') &= \frac{1}{2\pi(\lambda')^2}\int_{-1}^{1} Q_{ij}(\hat{\boldsymbol{x}}')f_j'(\Xi')d\Xi' - \frac{1}{2\pi}I_{ij}f_j'(\eta') \\ &\quad + O(\gamma'^{-1}), \quad (19a) \end{aligned}$$

where

$$\begin{aligned} I_{ij} &= \int_{-\gamma'(1+\eta')}^{\gamma'(1-\eta')}\left[K_0(\sqrt{i}r'')\left(\delta_{ij}+\frac{x_i''x_j''}{r''^2}\right)\right. \\ &\quad \left. - \frac{K_1(\sqrt{i}r'')}{\sqrt{i}r''}\left(\delta_{ij}-\frac{2x_i''x_j''}{r''^2}\right)\right]d\Xi'', \quad (19b) \end{aligned}$$

and $x_2''=\Xi''$, $x_3''=D'$, and $r''^2=\Xi''^2+\gamma'^2$. Hence, in this high-frequency limit, the leading-order inviscid flow depends upon the full width of the plate and requires a distribution of dipoles along its midplane, whereas viscous contributions are local to a given point. Although Eq. (19a) must be solved numerically, by discretizing into elements along the midplane and assuming the f_j' are constant on each element, this approach still offers substantial computational savings, since we can integrate the dipoles analytically over each element, thereby dispensing with the greatest overhead, numerical quadrature. We shall refer to this limit as the two-dimensional high-frequency thin-plate-theory (2D HFTPT) approximation. In Sec. V we shall compare the plate deflections calculated using this two-dimensional hydrodynamic loading against those computed using full three-dimensional flows.

B. Hydrodynamic wall screening [$\Delta \ll \min(1,R)$, $\gamma\Delta = O(1)$]

When the wall-plate separation distance is of similar size to the thin oscillatory Stokes layers on the solid surfaces ($\Delta \sim \gamma^{-1}$) and smaller than the smallest horizontal plate dimensions [$\Delta \ll \min(1,R)$], we expect the dominant drag contribution to come from an unsteady lubrication region between the wall and the plate. The flow in this gap can be examined by rescaling distances, velocities, and pressure as follows:

$$x_1=\tilde{x}_1, \quad x_2=\tilde{x}_2, \quad x_3=\Delta\tilde{x}_3,$$

$$u_1=\Delta^{-1}\tilde{u}_1, \quad u_2=\Delta^{-1}\tilde{u}_2, \quad u_3=\tilde{u}_3, \quad p=\Delta^{-3}\tilde{p}. \quad (20)$$

The leading-order flow is then governed by (dropping tildes)

$$i\tau^2 u_1 = -\frac{\partial p}{\partial x_1} + \frac{\partial^2 u_1}{\partial x_3^2}, \quad (21)$$

$$i\tau^2 u_2 = -\frac{\partial p}{\partial x_2} + \frac{\partial^2 u_2}{\partial x_3^2}, \quad \frac{\partial p}{\partial x_3}=0, \quad \nabla\cdot\boldsymbol{u}=0, \quad (22)$$

where $\tau=\gamma\Delta$, subject to the no-slip and no-penetration conditions

$$\boldsymbol{u}(x_1,x_2,0)=\boldsymbol{0}, \quad (23a)$$

$$\boldsymbol{u}(x_1,x_2,1)=iw(x_1,x_2)\hat{\boldsymbol{x}}_3. \quad (23b)$$

This is solved by

$$u_1\hat{\boldsymbol{x}}_1+u_2\hat{\boldsymbol{x}}_2 = \boldsymbol{A}e^{\sqrt{i}\tau x_3}+\boldsymbol{B}e^{-\sqrt{i}\tau x_3}-\frac{1}{i\tau^2}\nabla_s p, \quad (24a)$$

$$u_3 = \nabla_s\cdot\boldsymbol{B}\frac{e^{-\sqrt{i}\tau x_3}}{\sqrt{i}\tau} - \nabla_s\cdot\boldsymbol{A}\frac{e^{\sqrt{i}\tau x_3}}{\sqrt{i}\tau} + x_3\frac{\nabla_s^2 p}{i\tau^2} + C, \quad (24b)$$

where $\nabla_s=(\partial/\partial x_1,\partial/\partial x_2)$ and

$$\boldsymbol{A} = \frac{\boldsymbol{\nabla}_s p}{2i\tau^2}\left(\frac{1-e^{-\sqrt{i}\tau}}{\sinh\sqrt{i}\tau}\right), \tag{24c}$$

$$\boldsymbol{B} = \frac{\boldsymbol{\nabla}_s p}{2i\tau^2}\left(\frac{e^{\sqrt{i}\tau}-1}{\sinh\sqrt{i}\tau}\right), \quad C = \nabla_s^2 p\left(\frac{1-\cosh\sqrt{i}\tau}{i^{3/2}\tau^3\sinh\sqrt{i}\tau}\right). \tag{24d}$$

Imposing the no-penetration condition (23b) then provides a Poisson equation for the pressure,

$$\nabla_s^2 p = ik_0(\tau)w(x_1,x_2), \tag{25a}$$

$$k_0(\tau) = \frac{(\sqrt{i}\tau)^3\sinh\sqrt{i}\tau}{(2-2\cosh\sqrt{i}\tau+\sqrt{i}\tau\sinh\sqrt{i}\tau)}, \tag{25b}$$

where we specify the pressure at the plate edges to be zero, to leading order in Δ. In the quasisteady limit $\tau\to 0$, where vorticity diffuses over distances much greater than the gap thickness during one oscillation, $k_0(\tau)\to 12$ in agreement with the quasisteady results of Kim *et al.* [24]. Conversely, in the limit $\tau\to\infty$, which corresponds to the situation where the $O(\gamma^{-1})$ Stokes layers are much thinner than the plate-wall gap, $k_0(\tau)\to i\tau$. Hence, by Eqs. (20) and (25), $p=O(\gamma^2\Delta^{-1})$, which is consistent with the results of Clarke *et al.* [12].

Determining the dynamics of the plate in this small-Δ limit therefore involves solving Poisson's equation for the pressure (25) alongside the elasticity equations (2):

$$\nabla^4 w - \omega^2 w = M\Omega\Delta^{-3}p, \tag{26a}$$

$$\nabla_s^2 p = ik_0(\tau)w. \tag{26b}$$

We shall describe the simplifications that this brings to the numerical computation in Sec. IV.

Moreover, when the plate is narrow in this small-separation limit ($\Delta \ll R \ll 1$) we can find the leading-order deflections and pressure asymptotically, by exploiting the fact that narrow beams show very little transverse bending, i.e., $w(\xi,\eta)=w(\xi)$. Rescaling $\eta=R\tilde{\eta}$, the pressure equation (25) takes the form

$$\frac{\partial^2 p}{\partial\tilde{\eta}^2} + R^2\frac{\partial^2 p}{\partial\xi^2} = iR^2k_0(\tau)w(\xi), \tag{27}$$

subject to $p(\xi,\pm 1)=0$. Expanding pressure in powers of R we obtain

$$p = p^{(0)} + Rp^{(1)} + R^2p^{(2)} + O(R^3), \tag{28}$$

where

$$p^{(0)} = p^{(1)} = 0, \quad p^{(2)} = \frac{i}{2}k_0(\tau)w^{(0)}(\xi)(\tilde{\eta}^2-1). \tag{29}$$

We should, however, note that the two-dimensional pressure solution $p^{(2)}$ given by Eq. (29) is unable to satisfy both zero pressure and nonzero deflection conditions at $\xi=0$ and 1 simultaneously. We therefore consider the clamped-end region where $\xi=O(R)$ by rescaling $\xi=R\tilde{\xi}$, which leaves us needing to solve

$$\frac{\partial^2 p^{(2)}}{\partial\tilde{\eta}^2} + \frac{\partial^2 p^{(2)}}{\partial\tilde{\xi}^2} = ik_0(\tau)w(0) \tag{30a}$$

for the nontrivial pressure contribution, subject to the boundary conditions

$$p^{(2)}(0,\tilde{\eta}) = p^{(1)}(\tilde{\xi},0) = 0, \tag{30b}$$

as well as tending toward the two-dimensional solution away from the edges

$$p^{(2)}(\tilde{\xi},\tilde{\eta}) \to \frac{i}{2}k_0(\tau)w(0)(\tilde{\eta}^2-1) \quad \text{as } \tilde{\xi}\to\infty. \tag{30c}$$

This Poisson equation can be solved by posing the inhomogeneous solution

$$p_I^{(2)} = \frac{i}{2}k_0(\tau)w(0)(\tilde{\eta}^2-1), \tag{31}$$

which matches the outer solution as $\tilde{\xi}\to\infty$, and then calculating the harmonic function which cancels the nonzero values of the pressure at $\tilde{\xi}=0$ and decays at large $\tilde{\xi}$,

$$\nabla^2 p_h^{(2)} = 0,$$

$$p_h^{(2)}(0,\tilde{\eta}) = \frac{i}{2}k_0(\tau)w(0)(1-\tilde{\eta}^2),$$

$$p_h^{(2)}(\tilde{\xi},1) = 0, \quad p_h^{(2)}\to 0 \quad \text{as } \tilde{\xi}\to\infty. \tag{32}$$

Separation of variables then gives us the clamped-end-region pressure near $\xi=0$,

$$p(\tilde{\xi},\tilde{\eta}) = ik_0(\tau)w(0)\left(\frac{(\tilde{\eta}^2-1)}{2} + \frac{16}{\pi^3}\sum_{\substack{k=1\\ k\ \text{odd}}}^{\infty}\frac{\sin[k\pi(1+\tilde{\eta})/2]e^{-k\pi\tilde{\xi}/2}}{k^3}\right). \tag{33}$$

A similar analysis gives the end-region pressure near $\xi=1$ and hence the pressure can be expressed as the following composite expansion:

$$p^{(2)}(\xi,\eta) = \frac{i}{2}k_0(\tau)w(\xi)(\eta^2-R^2)/R^2 + \frac{16ik_0(\tau)w(0)}{\pi^3}\sum_{\substack{k=1\\ k\ \text{odd}}}^{\infty}\frac{\sin[k\pi(R+\eta)/2R]e^{-k\pi\xi/2R}}{k^3} + \frac{16ik_0(\tau)w(1)}{\pi^3}\sum_{\substack{k=1\\ k\ \text{odd}}}^{\infty}\frac{\sin[k\pi(R+\eta)/2R]e^{-k\pi(1-\xi)/2R}}{k^3}. \tag{34}$$

In Sec. V A we compare hydrodynamic loadings obtained using this composite expression with those computed using 3D TPT, in the small-separation limit.

IV. NUMERICAL SCHEME

We solve the coupled 3D TPT equation (13) and plate equations (5) numerically by discretizing the plate into $N \times M$ equally sized panels, in the ξ and η directions, respectively, setting $\xi_m = m/N$ and $\eta_k = kR/M$. We assume that the Stokeslet distribution $\boldsymbol{f}$ is uniform over each panel. The elastohydrodynamics can then be approximated by the $(5N \times M) \times (5N \times M)$ system

$$\boldsymbol{\Pi}_I \begin{pmatrix} \boldsymbol{Y}_I \\ \boldsymbol{F}_I \end{pmatrix} + \boldsymbol{\Pi}_0 \boldsymbol{Y}_0 = \boldsymbol{0}, \tag{35}$$

where

$$\boldsymbol{Y}_I = (w(\xi_1, \eta_1), \ldots, w(\xi_N, \eta_1), \ldots, w(\xi_1, \eta_M), \ldots, w(\xi_N, \eta_M), v(\xi_1, \eta_1), \ldots, v(\xi_N, \eta_1), \ldots, v(\xi_1, \eta_M), \ldots, v(\xi_N, \eta_M)) \tag{36}$$

contains values of w and v at internal points on the plate,

$$\boldsymbol{F}_I = (f_1(\xi_1, \eta_1), f_2(\xi_1, \eta_1), f_3(\xi_1, \eta_1), \ldots, f_1(\xi_N, \eta_1), f_2(\xi_N, \eta_1), f_3(\xi_N, \eta_1), \ldots, f_1(\xi_1, \eta_M), f_2(\xi_1, \eta_M), f_3(\xi_1, \eta_M), \ldots, f_1(\xi_N, \eta_M), f_2(\xi_N, \eta_M), f_3(\xi_N, \eta_M)) \tag{37}$$

contains internal values of $\boldsymbol{f}$, while

$$\boldsymbol{Y}_0 = (w(1, \eta_1), \ldots, w(1, \eta_M), w(\xi_1, 1), \ldots, w(\xi_N, 1), w(\xi_1, -1), \ldots, w(\xi_N, -1), v(1, \eta_1), \ldots, v(1, \eta_M), v(\xi_1, 1), \ldots, v(\xi_N, 1), v(\xi_1, -1), \ldots, v(\xi_N, -1), v(0, \eta_1), \ldots, v(0, \eta_M)) \tag{38}$$

consists of the boundary values of w and v (where the matrix $\boldsymbol{\Pi}_0$ augments $\boldsymbol{Y}_0$ with zeros in the necessary places). The values in $\boldsymbol{Y}_0$ are determined by the boundary conditions given in (6), which produce a set of $(2N+3M)$ equations relating internal points to boundary values

$$\boldsymbol{M}_1 \boldsymbol{Y}_I + \boldsymbol{M}_2 \boldsymbol{Y}_0 = \boldsymbol{B}, \tag{39}$$

where $\boldsymbol{M}_1, \boldsymbol{M}_2$ contain the finite-difference approximations to conditions on deflection derivatives in (6) (using three-point uniformly spaced central differencing) and $\boldsymbol{B}$ contains the relevant boundary conditions. Hence

$$\boldsymbol{Y}_0 = \boldsymbol{M}_2^{-1} \boldsymbol{B} - \boldsymbol{M}_2^{-1} \boldsymbol{M}_1 \boldsymbol{Y}_I, \tag{40}$$

giving, on substitution into (35),

$$\boldsymbol{\Pi}_I \begin{pmatrix} \boldsymbol{Y}_I \\ \boldsymbol{F}_I \end{pmatrix} - \boldsymbol{\Pi}_0 \boldsymbol{M}_2^{-1} \boldsymbol{M}_1 \boldsymbol{Y}_I + \boldsymbol{\Pi}_0 \boldsymbol{M}_2^{-1} \boldsymbol{B} = \boldsymbol{0}, \tag{41}$$

where

$$\boldsymbol{\Pi}_I = \begin{pmatrix} \boldsymbol{E} & \boldsymbol{J}_1 \\ \boldsymbol{J}_2 & \boldsymbol{G} \end{pmatrix}. \tag{42}$$

Here

$$\boldsymbol{E} = \begin{pmatrix} \boldsymbol{L} & -\boldsymbol{I} \\ -\omega^2 \boldsymbol{I} & \boldsymbol{L} \end{pmatrix} \tag{43}$$

is the discretized elasticity operator in Eq. (5) and $\boldsymbol{G}$ is the discretized hydrodynamic operator in Eq. (13), whose entries are defined by

$$G_{\alpha,\beta} = \frac{1}{8\pi} \int_{\xi_{m-1}}^{\xi_m} \int_{\eta_{k-1}}^{\eta_k} \bar{S}_{ij}(\boldsymbol{x}_M, \boldsymbol{X}_M; \gamma, \Delta) d\xi \, d\eta, \tag{44}$$

where the values of $1 \leqslant \alpha, \beta \leqslant 3N \times M$ determine the force and velocity component indices $1 \leqslant i, j \leqslant 3$ through the equalities

$$\alpha = 3(k' - 1)N + 3(m' - 1) + i,$$

$$\beta = 3(k - 1)N + 3(m - 1) + j, \tag{45}$$

where $1 \leqslant k, k' \leqslant M$, $1 \leqslant m, m' \leqslant N$, and (k', m') and (k, m) index the panels on which velocity and force, respectively, are being evaluated. $\boldsymbol{L}$ is the finite-difference approximation to the Laplacian, $\boldsymbol{I}$ is the $(N \times M) \times (N \times M)$ identity matrix, $\boldsymbol{J}_1$ is the $(N \times M) \times (N \times M)$ zero matrix other than $-M\Omega$ values in $[k, 3(k-1)+3]$-indexed entries, as is $\boldsymbol{J}_2$ except for $-i$ values in $[3(k'-1)+3, k']$-indexed entries $(1 \leqslant k, k' \leqslant N \times M)$. Solving this linear system by Gaussian elimination provides the plate deflection and the Stokeslet distribution of $\boldsymbol{f}$ over the plate. Convergence is verified by solving on 30×30 and 50×50 meshes, to ensure grid independence.

Computing the rigid-plate hydrodynamics using 3D TPT amounts to solving the $(3N \times M) \times (3N \times M)$ system

$$i\boldsymbol{W} = \boldsymbol{G}\boldsymbol{F}_I, \tag{46}$$

where $\boldsymbol{W} = (0, 0, w(\xi_1, \eta_1), \ldots, 0, 0, w(\xi_N, \eta_1), \ldots, 0, 0, w(\xi_1, \eta_M), \ldots, 0, 0, w(\xi_N, \eta_M))$. An analogous boundary-element method (BEM) scheme is constructed for flow computations based on the three-dimensional boundary-integral formulation (11), but here the system is $[3N \times M + 3N \times K + 3K \times M]^2$ in size as the ends $(\xi = 0, 1)$ and sides $(\eta = \pm R)$ of the plate must also be covered by $N \times K$ and $M \times K$ panels, respectively. Coupling the 3D BEM with the elastic dynamics therefore requires solving a $\{5 \times [N \times M + N \times K + M$

$\times K]\}^2$-sized linear system, compared with the $(5N\times M)\times(5N\times M)$ system generated when using 3D TPT, clearly demonstrating the computational savings available.

Small wall-separation limit ($\Delta\sim\gamma^{-1}\ll 1$)

The most time-consuming element of Eq. (35) is evaluation of the hydrodynamic matrix $\boldsymbol{G}$ in $\boldsymbol{\Pi}_I$. In the small-wall-separation limit, however, the fluid loading can be approximated using a lubrication theory assumption (Sec. III B). Under these circumstances the discretized equation (41) simplifies to the $(2N\times M)\times(2N\times M)$ system

$$\boldsymbol{\Pi}_I'\begin{pmatrix}\boldsymbol{Y}_I\\ \boldsymbol{P}\end{pmatrix}-\boldsymbol{\Pi}_0\boldsymbol{M}_2^{-1}\boldsymbol{M}_1\boldsymbol{Y}_I+\boldsymbol{\Pi}_0\boldsymbol{M}_2^{-1}\boldsymbol{B}=\boldsymbol{0}, \tag{47}$$

where

$$\boldsymbol{P}=(p(\xi_1,\eta_1),\ldots,p(\xi_N,\eta_1),\ldots,p(\xi_1,\eta_M),\ldots,p(\xi_N,\eta_M)) \tag{48}$$

is the fluid pressure on the plate and

$$\boldsymbol{\Pi}_I'=\begin{pmatrix}\boldsymbol{E} & \boldsymbol{J}_3\\ \boldsymbol{J}_4 & \boldsymbol{L}\end{pmatrix}, \tag{49}$$

with

$$\boldsymbol{J}_3=-M\Omega\begin{pmatrix}\boldsymbol{I}\\ \boldsymbol{0}\end{pmatrix},\quad \boldsymbol{J}_4=-ik_0(\tau)(\boldsymbol{I}\ \boldsymbol{0}) \tag{50}$$

[$\boldsymbol{0}$ is the $(N\times M)\times(N\times M)$ zero matrix]. $\boldsymbol{\Pi}_I'$ captures the fluid-structure interactions [recalling that $k_0(\tau)$ is given by Eq. (25b)].

V. RESULTS

We begin by considering the purely fluid-mechanical aspects of the dynamics, by taking the plate to be rigid (Sec. V A). In particular, we examine the effectiveness of the three-dimensional thin-plate-theory formulation (13) and the two-dimensional character of the flow for narrow plates under certain situations. Elastic plates are then covered in Sec. V B, where deflections of finite-width elastic plates identical to the cantilevers used in the AFM experiments of Chon *et al.* [25] are computed using both three- and two-dimensional hydrodynamical loading.

A. Rigid plate

We first illustrate the ability of the various forms of TPT [3D TPT (13), 2D TPT (16), and (at high frequencies) 2D HFTPT (19a) and (19b)] to correctly estimate the hydrodynamic loading on a rigid plate by comparing their predictions with full BEM computations (11) and (14) (Sec. V A 1).

Having established the reliability of 3D TPT, we then use it to illustrate the extent to which the hydrodynamic loading on a narrow plate that is oscillating at high frequencies can be approximated using the 2D BEM (Sec. V A 2). Separately (Sec. V A 3), we use 3D TPT to illustrate the promotion of flow two-dimensionality through decreased wall-plate separation distances, where lubrication theory (26) is expected to provide a reliable estimate of the hydrodynamic loading. The range of validity for these effects are then quantified through profiles of the overall drag exerted on the plate as functions of frequency and separation distance (Sec. V A 4); these quantitative results will provide valuable reference data for those wishing to choose an appropriate hydrodynamic model for a given application.

1. TPT validation

Figure 2 illustrates the ability of 3D TPT (13), shown with a wire mesh surface, to approximate accurately the additive contribution of Stokeslet distributions on the upper and lower sides of the plate computed using the full 3D boundary-integral flow formulation (11) (shaded surface) for both unbounded flow [Figs. 2(a) and 2(b)] and when the plate is close to the wall [$\Delta=0.1$, Figs. 2(c) and 2(d)]. (Note that for a rigid plate, symmetry of the flow about $\xi=0.5$ and $\eta=0$ means that it is sufficient to plot Stokeslet profiles in the quadrant $0.5\leqslant\xi\leqslant 1$, $-R\leqslant\eta\leqslant 0$.) Since the fluid loading on the plate is given by this additive contribution (the much smaller side edges contribute little to the overall loading for a sufficiently thin plate; see Eq. [12]), TPT represents a useful and convenient simplification. As an indication of the computational savings offered by the TPT formulation, a full 3D BEM computation with no wall using 20×20 panels for horizontal surfaces and 20×10 panels for vertical surfaces runs in about 7200 s on a 1.7 GHz desktop PC, compared with 72 s for 3D TPT using 20×20 resolution on the same machine. At the same spatial resolution, when the wall is present and image Stokeslets are used (which are distributed over the wall and therefore require additional numerical quadrature; see Appendix A) the computational time increases to 39 316 s for 3D BEM, compared with 1343 s for 3D TPT. In both cases, the TPT run time is just a few percent of that required by 3D BEM. The consequence for calculating fluid-structure interactions is that prohibitively large numerical schemes that rely on the 3D BEM can be reduced to a manageable size (for conventional desktop PC processing power) through the use of 3D TPT (as well as the reductions in the overall size of the system as discussed in Sec. IV).

As we will shortly identify situations in which the flow can be considered to be two dimensional through screening effects, it proves useful to perform an analogous validation of 2D TPT. Figure 3 shows the two-dimensional Stokeslet distribution along the plate's centerline for the cases where [Figs. 3(a) and 3(b)] $\Delta'=100$, $\gamma'=3$, [Figs. 3(c) and 3(d)] $\Delta'=1$, $\gamma'=1$, and [Figs. 3(e) and 3(f)] $\Delta'=100$, $\gamma'=50$ (recalling that $\gamma=\gamma'/R$, $\Delta=R\Delta'$, so for a narrow plate $\gamma\gg\gamma'$, $\Delta\ll\Delta'$). Figures 3(a)–3(d) clearly demonstrate that the additive sum of the upper and lower Stokeslet distributions in the full 2D BEM computations (14) (circular markers) is well approximated by the predictions of 2D TPT (16) (full line), even when the upper (dashed lines) and lower profiles (dotted lines) differ due to the presence of a nearby wall [Figs. 3(c) and 3(d)].

Furthermore, at high frequencies of oscillation the 2D TPT formulation can be simplified still further. The effectiveness of 2D HFTPT (19a) and (19b) is demonstrated in Figs. 3(e) and 3(f), which compares the two-dimensional high-

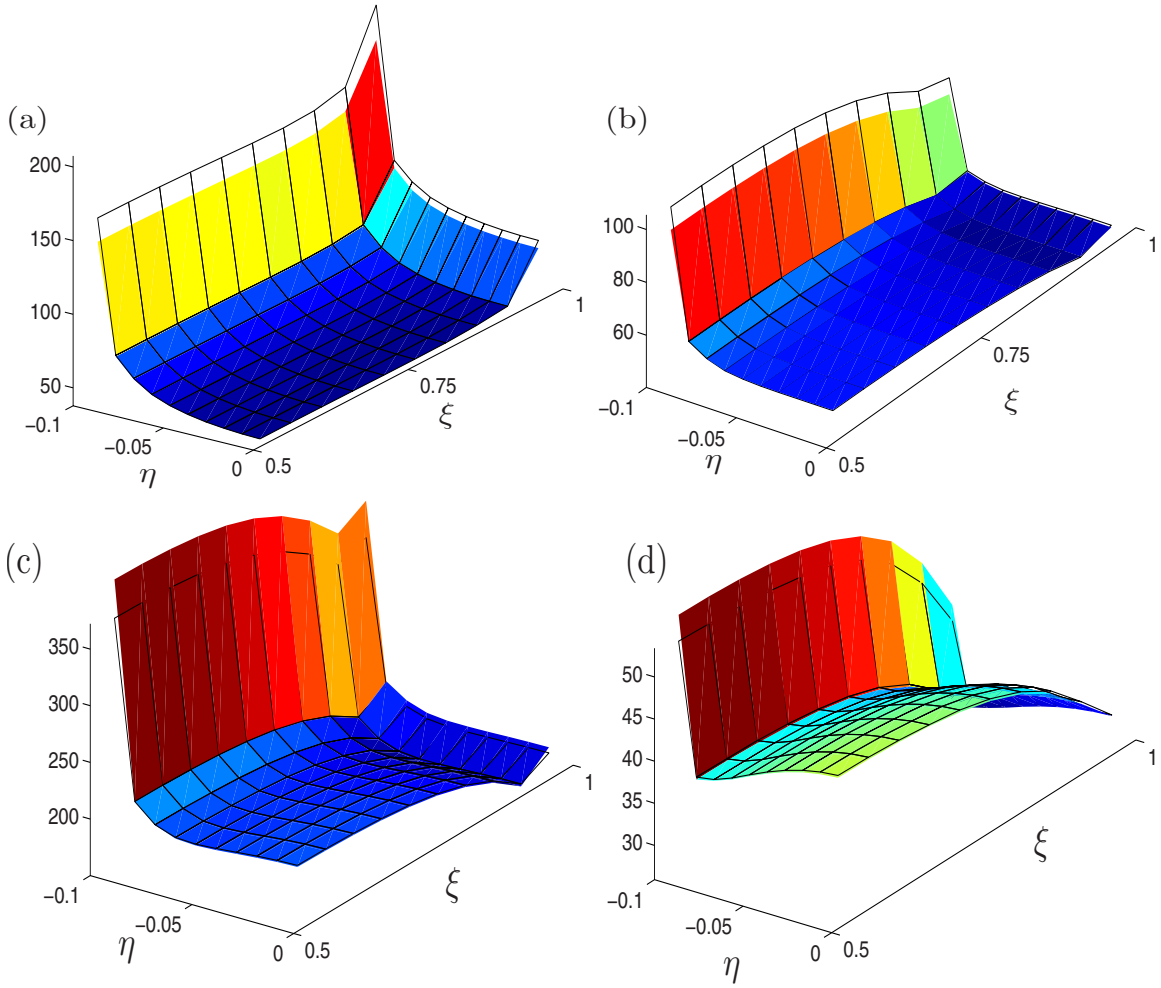

FIG. 2. (Color online) Shaded surfaces shows the real (a), (c) and imaginary (b), (d) parts, respectively, of the vertical component of the Stokeslet distribution f_3 computed using 3D TPT (13). The line meshes show the additive contributions of the Stokeslet profiles on the upper and lower surfaces $g_3|_{S_U} + g_3|_{S_L}$, calculated by numerically solving the full 3D boundary-integral equation (11). Profiles correspond to a plate with thickness $D=10^{-3}$ which is oscillating with $\gamma=1$ when (a), (b) the wall is absent ($\Delta \gg 1$) and (c), (d) $\Delta=0.1$.

frequency thin-plate Stokeslet distribution against that computed using the more general 2D TPT method (16). Away from the sides ($\eta=\pm R$, where the Stokeslet distribution and its derivatives are singular) 2D HFTPT is seen to perform well in capturing the additive Stokeslet distribution, which is highly nonuniform due to the sensitivity of inviscid flow to plate geometry. Under these conditions, the lack of a need for numerical quadrature in the 2D HFTPT scheme results in a very fast method for computing the hydrodynamic loading on the plate.

2. Frequency screening

We now study the 3D TPT (13) profiles obtained in the absence of the wall. Near $\xi=0$ and 1 there are three-dimensional effects associated with flows around the ends of the plate. The range of these three-dimensional flows is determined both by the frequency of oscillation and the width of the plate.

At low frequencies the length scale over which vorticity diffuses (γ^{-1}) is much larger than the length of the plate and so the three-dimensional flows generated at the ends are felt across the whole plate. Hence, in this regime, the cross-sectional Stokeslet profile differs from the 2D BEM predictions (14), as demonstrated by Figs. 4(a) and 4(b) which show the midplane Stokeslet distribution f_3 for a rigid plate oscillating at a low frequency ($\gamma=0.01$).

When we increase the frequency of oscillation (again in the absence of a wall) so that $1 \ll \gamma$ [Figs. 4(c) and 4(d)] the range over which the vorticity generated by three-dimensional flows at the ends of the plate can diffuse is limited to $O(\gamma^{-1})$ distances and so the reach of the three-dimensional flow is determined by inviscid effects. Since the inviscid three-dimensional flows around the ends of the plate scale with its width R, when the plate is narrow ($R \ll 1$) their range is limited and the flow over much of the plate is effectively two-dimensional. Under these circumstances a Stokeslet cross section at $\xi=0.5$ is seen to give good agreement with 2D BEM computations, as illustrated by Figs. 4(c) and 4(d), which correspond to $\gamma=100$ and $R=0.1$. We shall refer to this effect as frequency screening. Deviations from this profile occur only at $O(R)$ distances from $\xi=1$ (and, by symmetry, $\xi=0$).

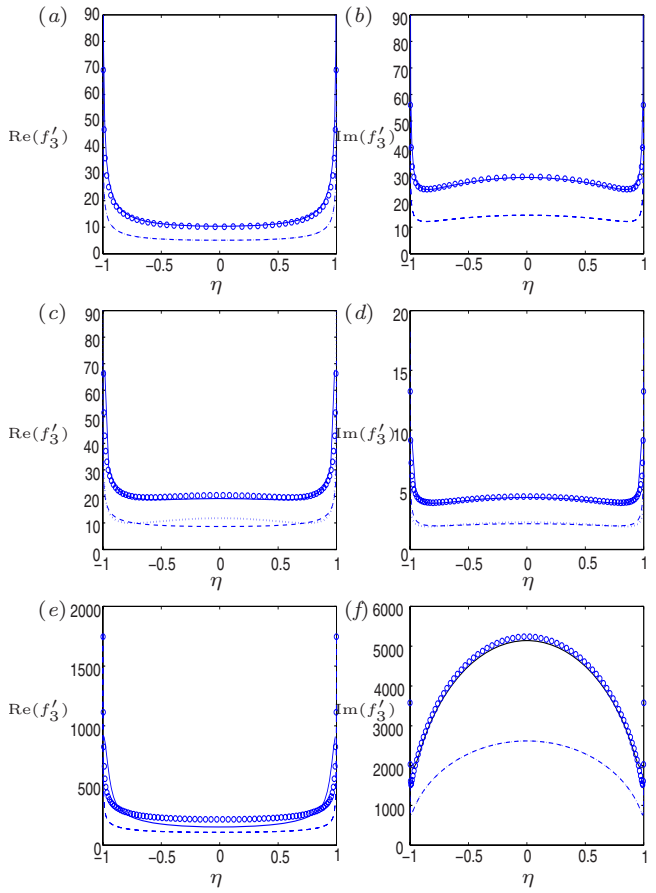

FIG. 3. (Color online) Two-dimensional flow approximations: real (a), (c), (e) and imaginary (b), (d), (f) parts of the vertical component of Stokeslet strength f_3' for a thin two-dimensional plate ($D=10^{-2}$) when (a), (b) $\Delta'=100$, $\gamma'=3$, (c), (d) $\Delta'=1$, $\gamma'=1$, and (e), (f) $\Delta'=100$, $\gamma'=50$. Dashed lines in (a)–(f) show the Stokeslet distribution f_3' on the top of the plate while dotted lines indicate distributions on the plate bottom, both computed using the 2D BEM (14). [Note that dashed and dotted lines coincide in (a), (b), (e), and (f).] Circular markers denote their additive contribution. Full lines in (a)–(d) show the predictions of 2D TPT (16), while in (e), (f) they show the predictions of 2D HFTPT (19a) and (19b).

Close to both the sides and ends of the plate we expect an $O(s^{-\beta_0})$ singularity in the Stokeslet profile, where $\beta_0 \approx 0.5$ for viscous flow around a flat plate [19], although the flows away from these very localized regions differ depending on whether the edge is a plate side or a plate end [as observed in Figs. 4(a)–4(d)]. The flow near the corners is more complex, with no simple canonical flow providing the strength of the singularity, although the profiles suggest that this corner flow is more singular than along the edges.

3. Wall screening

The presence of a nearby wall promotes two-dimensionality in the flow, even at low frequencies of oscillation, where we expect frequency screening to be absent. Figures 4(e) and 4(f) reveal that the discrepancy which exists at large separation distances between the 3D TPT profile across $\xi=0.5$ and the predictions of 2D BEM [$\Delta=100$, Fig. 4(e)], disappears once the plate is brought sufficiently close to the wall [$\Delta=0.1$, Fig. 4(f)]. Under these circumstances we expect lubrication theory (26) to approximate the fluid loading effectively, and the drag results of Sec. V A 4 will reveal the extent to which this holds true.

4. Drag

By integrating the vertical component of the Stokeslet distribution f_3 over the plate surface we can obtain the hydrodynamic drag that acts on the plate.

Figure 5 plots drag as a function of γ, in the absence of a wall and for several different aspect ratios, to demonstrate the impact of frequency screening on the drag. Profiles are computed using 2D (markers) and 3D (full line) TPT as well as 2D BEM (14) (dashed line). 2D TPT and BEM predictions are seen to be always in agreement, thereby further confirming the validity of the TPT approximation. In contrast, we see significant divergence between two- and three-dimensional predictions for drag moduli below $\gamma \approx 1$ and for drag phase below $\gamma \approx 10$, due to the increasing influence of three-dimensionality via long-ranged viscous effects. When the frequency of oscillation is increased, the two- and three-dimensional drags initially converge, as viscous end effects become shorter ranged. However, finite-width inviscid effects become stronger as R increases and these ultimately lead to the small divergence between the two- and three-dimensional drags at high frequencies. Understandably the magnitude of this divergence is seen to be a function of plate width.

The influence of the wall is charted in Figs. 6 and 7, where the drag amplitudes and phases are plotted against separation distance Δ for different oscillation frequencies and plate aspect ratios. In all cases we observe an agreement between 3D TPT, 2D BEM, and 3D lubrication theory at sufficiently small Δ, due to wall screening effects. In the narrow plate limit (Fig. 6) we use the asymptotic expression (34), thereby validating its effectiveness against 3D TPT and 2D BEM. The validity of 3D lubrication theory is seen to become questionable once $\Delta \approx 1$, at which point the predictions of 2D BEM and 3D TPT also begin to differ for a plate of unit aspect ratio (Fig. 7).

When the plate is narrow ($R=0.1$) but the frequency of oscillation is low [$\gamma=0.1$; Figs. 6(a) and 6(b)], however, 2D BEM and 3D TPT are seen to agree relatively well until $\Delta \approx 10$, at which point the drag phases begin to diverge. At moderate oscillation frequencies [$\gamma=1$, Figs. 6(c) and 6(d)] the agreement is seen to persist even for $\Delta \gg 1$. This is somewhat surprising as the oscillation frequency should still be too low for frequency screening effects, which we do expect to account for the large-separation agreement when $\gamma=10$ [Figs. 6(c) and 6(d). We note also that the value of Δ at which the drag attains its unbounded limit decreases at higher values of γ, thereby quantifying how the range of the wall's influence diminishes with increasing oscillation frequencies.

B. Elastic plate

We now consider nonrigid plates, where deflections governed by Eq. (5) are coupled to the fluid dynamics, as gov-

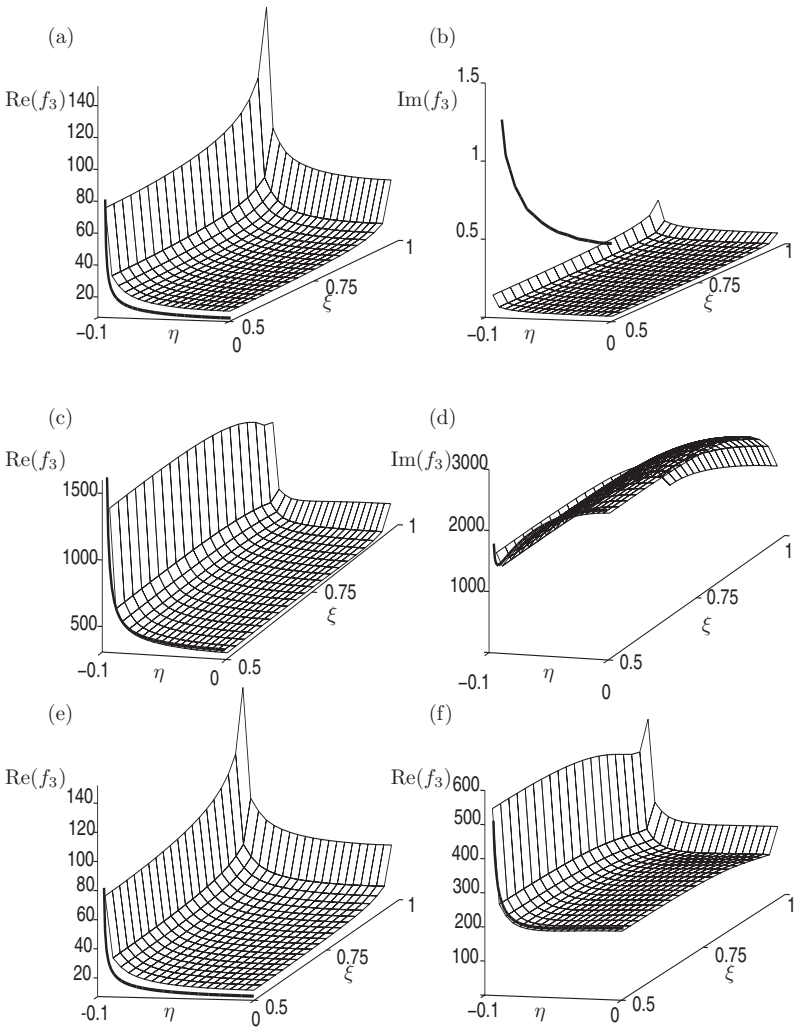

FIG. 4. Real (a), (c), (e), (f) and imaginary (b), (d) parts of the vertical component of the Stokeslet distribution f_3 for a rigid plate. These profiles are computed using three-dimensional thin-plate theory (13) when (a), (b) $\gamma=0.01$, $R=0.1$, $D=10^{-3}$, $\Delta \gg 1$, (c), (d) $\gamma=100$, $R=0.1$, $D=10^{-3}$, $\Delta \gg 1$, (e) $\gamma=0.01$, $R=0.1$, $D=10^{-3}$, $\Delta=100$, and (f) $\gamma=0.01$, $R=0.1$, $D=10^{-3}$, $\Delta=0.1$. (Imaginary parts are negligible when $\gamma=0.01$.) The thick line gives the two-dimensional loading F' as predicted using 2D BEM (15).

erned by Eq. (13) or Eq. (14). The results presented here will explore the consequencies of the above fluid-dynamical phenomena on both the driven responses of elastic plates, as well as their thermal spectra. We examine two plates with the same material properties as those used in the AFM experiments of Chon *et al.* [25], the specifications of which are listed in Table I alongside the corresponding nondimensional quantities Ω and M in both air and water. Note that the natural frequency ω_0 is related to the resonant frequency in vacuum ω_v, as defined by Chon *et al.* [25], through the relationship

$$\omega_v = c_1^2 \sqrt{(1-\nu_p^2)}\omega_0$$

($c_1 \approx 1.875$) which was found to take the values $\omega_v = 2\pi \times 17.52$ kHz $= 110.1 \times 10^3$ rad s^{-1} for C1 and $\omega_v = 2\pi \times 70.26$ kHz $= 441.5 \times 10^3$ rad s^{-1} for C2 [25]. Hence C1 has $\omega_0 = 32.8 \times 10^3$ rad s^{-1} and C2 has $\omega_0 = 131.6 \times 10^3$ rad s^{-1}.

We consider these plates in both air and water, in the absence of a wall, when driven externally (Fig. 8) and thermally (Fig. 9). We begin by noting by inspection how the quality factor increases with plate width (in agreement with earlier studies [26]) but decreases as we move from air (dynamic viscosity $\mu = \nu\rho = 1.8 \times 10^{-5}$ kg m^{-1} s^{-1}) to water (dynamic viscosity $\mu = \nu\rho = 1 \times 10^{-3}$ kg m^{-1} s^{-1}), as we would expect.

In keeping with the main theme of this study, however, our principal interest lies in the influence of three-dimensional flows on the elastic response of the plate under external (Fig. 8) and thermal (Fig. 9) driving. This is analyzed by computing the plate response subject to hydrodynamic loading provided by either 3D TPT or 2D BEM [shown by thick solid lines and circular markers, respectively, in panels (iii) of Figs. 8(a)–8(d) and 9(a)–9(d)]. In air [Figs. 8(a)(iii), 8(b)(iii), 9(a)(iii), and 9(b)(iii)] we observe that the responses computed using 2D BEM hydrodynamics are virtually indistinguishable from those produced using 3D TPT. In water [Figs. 8(c)(iii), 8(d)(iii), 9(c)(iii), and 9(d)(iii)], however, there are noticeable discrepancies. We note that the use of 2D BEM hydrodynamics leads to a resonant peak with a slightly lower frequency and marginally larger amplitude. Although away from the ends of the plate (i.e., at $\xi=0.5$) we observe a good agreement between 3D TPT and 2D BEM [Figs. 8(c)(i), 8(d)(i), 9(c)(i), and 9(d)(i)] longitudinal profiles taken along $\eta=0$ [Figs. 8(c)(ii), 8(d)(ii), 9(c)(ii), and 9(d)(ii)] illustrate the influence of three-dimensional end flows. Although the range of these end flows are comparable in both water and air (compare panels (a)(ii) and (b)(ii) with panels (c)(ii) and (d)(ii) in both Figs. 8

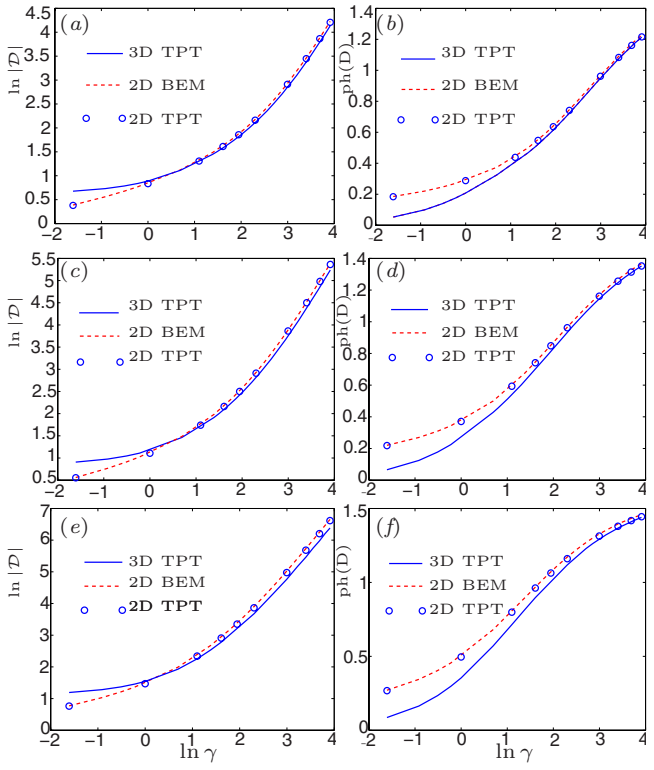

FIG. 5. (Color online) Effectiveness of frequency screening in terms of overall hydrodynamic drag $\mathcal{D}$ exerted on the plate. Modulus (a), (c), (e) and phase (b), (d), (f) of the 3D TPT drag (full line) evaluated over a range of γ, compared with the 2D BEM drag (dashed line) and the 2D TPT formulation (markers), when (a), (b) $R=0.1$, (c), (d) $R=0.2$, and (e), (f) $R=0.4$, in the absence of a wall.

and 9), which is perhaps to be expected considering that the resonant peaks in both air and water correspond to comparable values of γ^{-1} (approximately 0.03 in air and 0.01 in water), the larger magnitude of the hydrodynamic loading experienced by plates immersed in water likely increases the overall influence of these end regions.

VI. CONCLUSIONS

We have examined the dynamics of a fluid-immersed thin elastic plate oscillating at high frequencies and small amplitudes, close to a plane wall. Initially we considered a rigid, non-deformable plate, in order to focus on fluid effects and to extend earlier two-dimensional theory [12]. The limiting cases of high oscillation frequencies and small wall separation distances, where two-dimensional results are recovered, were therefore of particular interest. The plate was then allowed to deform elastically, enabling us to treat viscous-damped microscopic plates of the type often encountered in modern microdevices.

A. Rigid plates

For a plate of arbitrary thickness, the flow has a boundary-integral representation, which distributes oscillatory image Stokeslets over the entire plate surface. However, in the limiting case of a thin plate we approximated the flow

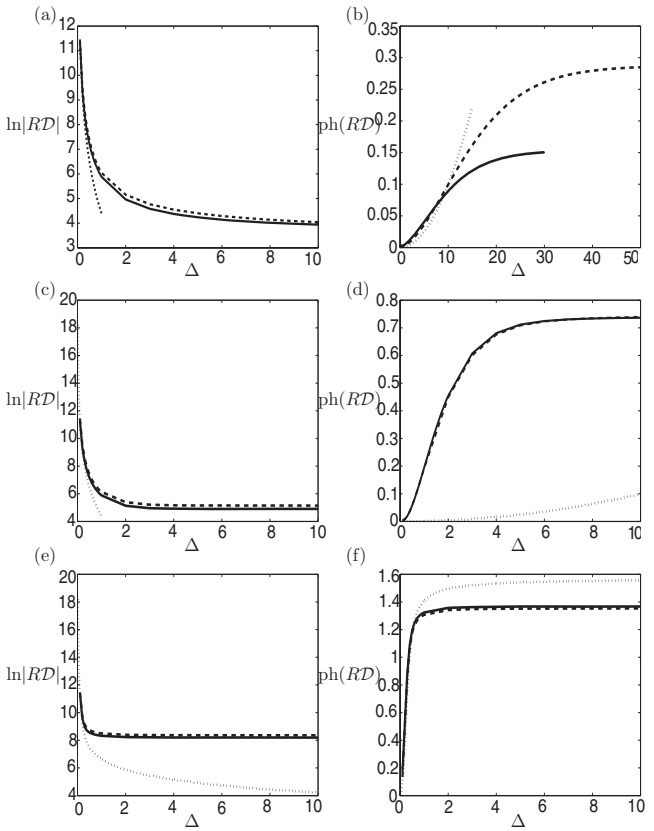

FIG. 6. Amplitude (a), (c), (e) and phase (b), (d), (f) of the drag $\mathcal{D}$ (scaled on R) on a three-dimensional plate, with uniformly prescribed velocity $w=1$ and aspect ratio $R=0.1$, plotted as a function of Δ when (a), (b) $\gamma=0.1$, (c), (d) $\gamma=1$, and (e), (f) $\gamma=10$. Drag is computed using 3D TPT (13) (full line), 2D BEM (dashed line), and narrow-plate lubrication approximation (34) (dotted line).

using a single distribution of Stokeslets over the plate's midplane, a formulation we termed thin-plate theory. This 3D TPT formulation extends the formulations proposed by Tuck [27] and Green and Sader [4] for the limiting case of a thin plate, which use a stream-function–pressure representation for the flow and hence are restricted to consideration of two-dimensional flows.

The validity of TPT in both two and three dimensions was verified by direct comparison with BEM predictions [Figs.

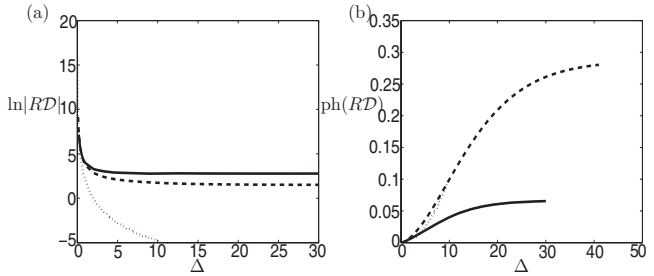

FIG. 7. Amplitude (a) and phase (b) of the drag $\mathcal{D}$ (scaled on R) on a three-dimensional plate, with uniformly prescribed velocity $w=1$ and aspect ratio $R=1$, plotted as a function of Δ when $\gamma=0.1$. Drags are computed using 3D TPT (13) (full line), 2D BEM (dashed line), and 3D lubrication theory (dotted line) (26).

TABLE I. Material properties of the two undoped and uncoated single-crystal silicon AFM cantilevers C1 and C2, as considered in the experiments of Chon *et al.* [25]. Specifications include length L^*, natural radial frequency ω_0, resonant frequency in vacuum, ω_v, and Youngs modulus E. Both C1 and C2 have widths $2R^*=28$ μm and thicknesses $2D^*=2$ μm, leading to respective nondimensional thicknesses $2D=0.005$ and $2D=0.01$. Nondimensional quantities Ω and M in both air ($\rho=1.2$ kg m^{-3}, $\nu=1.5\times10^{-5}$ m^2/s) and water ($\rho=1000$ kg m^{-3}, $\nu=10^{-6}$ m^2/s) are also shown. In all cases we take the plate to have Poisson ratio $\nu_p=0.3$ and density $\rho_c=2320$ kg m^{-3}.

	L^* (μm)	R	ω_0 (10^3 rad s^{-1})	ω_v	E (GPa)	Ω (air)	Ω (water)	M (air)	M (water)
C1	397	0.035	32.8	110.1	170	0.103	85.560	3×10^{-3}	2×10^{-4}
C2	197	0.071	131.6	441.5	165	0.051	42.457	3×10^{-3}	2×10^{-4}

2(a)–2(d) and 3(a)–3(d)], with TPT requiring just 1% of the computational time demanded by the BEM (at the minimum spatial resolution for numerical convergence). Importantly, when the plate was near to the wall, the additive contribution from differing profiles on the upper and lower surfaces (which provide the dominant fluid loading on the plate) computed using BEM was correctly reproduced using TPT.

We were able to verify that at high frequencies the flow generated by a narrow plate assumed a two-dimensional profile which could be accurately estimated using 2D BEM [Figs. 4(c) and 4(d)]. The proven agreement between 2D TPT and 2D BEM therefore permits the flow over much of the three-dimensional plate to be described using just a single line distribution of Stokeslets in the high-frequency regime, thereby facilitating further considerable computational savings.

At especially high frequencies, additional simplifications to the flow formulation were shown to be possible. In two-dimensional high-frequency thin-plate theory, viscous effects were captured by a local coefficient and all nonlocal phenomena were contained within a dipole distribution, which could be treated analytically, thereby eliminating the need for numerical quadrature. Figures 3(e) and 3(f) demonstrate the effectiveness of 2D HFTPT by comparing with profiles obtained using the 2D BEM formulation. Only near the plate edges did 2D HFTPT differ noticeably from 2D BEM, suggesting the need for higher-order corrections in γ. For a 100-μm-sized microdevice component immersed in water, this high-frequency regime corresponds to frequencies in the order of 1 MHz, i.e., within the operating range of modern AFMs.

The tendency of strong wall effects to promote two-dimensionality in the flow was also confirmed. The presence of the wall was accounted for in the 3D TPT formulation through the use of three-dimensional oscillatory image Stokeslets (see Appendix A). Figures 4(e) and 4(f) demonstrated that, at low frequencies of oscillation, where we would not expect any frequency screening, the flow away from the end of a narrow plate was largely two dimensional provided that the wall was sufficiently close.

These two-dimensional limits were quantified in the profiles of overall drag on the plate as a function of frequency (Fig. 5) and separation distance (Fig. 6). At $\gamma=0.1$, the 2D BEM predictions are seen to be reasonably accurate up to $\Delta\approx10$ when the plate was narrow ($R=0.1$), but only to $\Delta\approx1$ when the plate was square ($R=1$). However, when $1\lesssim\gamma$ and the plate was narrow, relatively good agreement was maintained at all values of Δ. In both cases, lubrication theory became reliable only at distances less than $\Delta\approx1$. In the absence of a wall, we see significant differences between 3D TPT and 2D BEM in the drag moduli for frequencies less than $\gamma\approx1$ and in the drag phase for frequencies below $\gamma\approx10$. We hope that these hydrodynamic findings will provide a useful reference source for a variety of different applications.

B. Elastic plates

Equipped with approximation techniques for the hydrodynamic loading, we were able to compute the damped elastic behavior in both air and water of flexible finite-width plates with material properties that matched those of the AFM cantilevers used in the experiments of Chon *et al.* (2000) [25]. Our attention focused on the influence of three-dimensional flows around the ends of the plate, which cannot be captured by two-dimensional fluid models. In air we observed that the elastic responses were entirely insensitive to the use of simpler two-dimensional hydrodynamic models in place of more involved three-dimensional hydrodynamic approximations. This, of course, validates the use of two-dimensional flow models when simulating the behavior of AFM cantilevers operating in air, as exploited by earlier theoretical studies [3,5]. When operating in water, however, our findings suggest that using two-dimensional fluid models instead of a fully three-dimensional treatment (that can capture the influence of hydrodynamic effects at the ends of the plate) introduces some degree of error into the predicted elastic responses. Although the range of end effects is largely comparable in both air and water near resonance (since the larger value of γ for a given frequency in water is countered by a drop in the frequency of the resonant peak), plates in water experience a larger overall fluid loading, which may cause three-dimensional hydrodynamic effects at the ends of the plate to be more influential than those present in air; hence a discrepancy that is only observed in water. In fact, we note that there are other recent reports of three-dimensional fluid effects [26,28,29], and it would be of great interest to see how these predictions match up with experiments specifically designed to explore these issues.

Of course, the practical impact of these findings on devices such as the AFM has to be measured against other

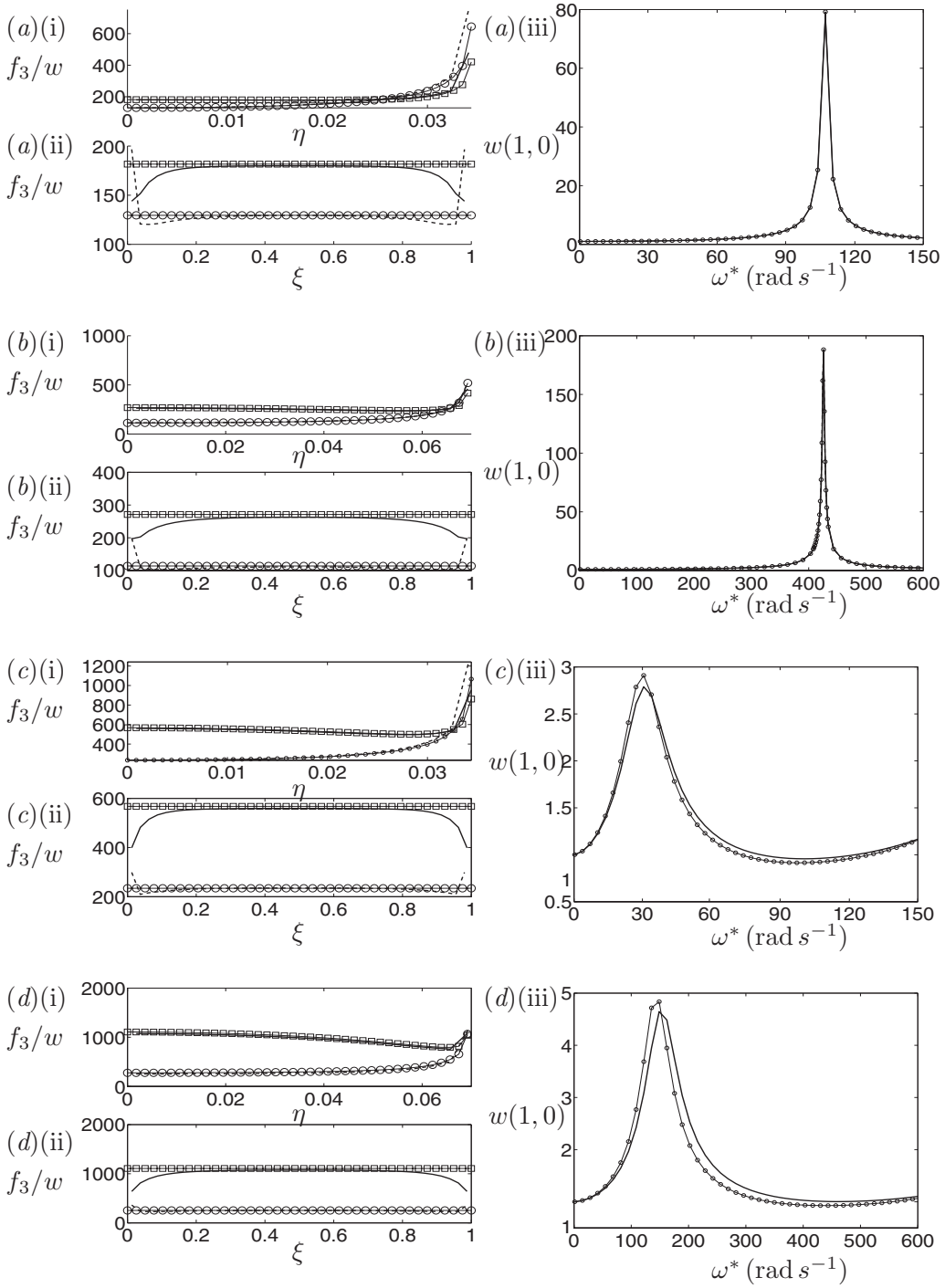

FIG. 8. Driven responses (iii) of plates C1 (a), (c) and C2 (b), (d) immersed in unbounded (a), (b) air and (c), (d) water, plotted against radial oscillation frequency ω^* and computed using the plate equations subject to 3D TPT (35) (thick solid lines) and 2D BEM hydrodynamic loading (circular markers). Panels (i) and (ii) show profiles of the real (solid lines) and imaginary (dashed lines) of components of 3D TPT loading across ξ=0.5 and η=0, respectively, and similarly for 2D BEM loading (square and circular markers for real and imaginary parts, respectively), at resonance.

effects, such as noise in the measurements, renormalization of the signal during postprocessing of the data, and parameter fitting for unknowns such as the cantilever spring constant, all of which may have dominated over this effect in earlier comparisons between theory and experiment. We should also note that certain device-specific geometrical features neglected here may also be important. For example, the AFM cantilever is often endowed with a tip at its unclamped end, as well as a support structure at the other end, which may alter the precise details of the hydrodynamics, although the degree to which this may or may not happen will likely be a function of the precise geometry of the additional features. As these features will vary from device to device and may necessitate full computational fluid dynamics (CFD)

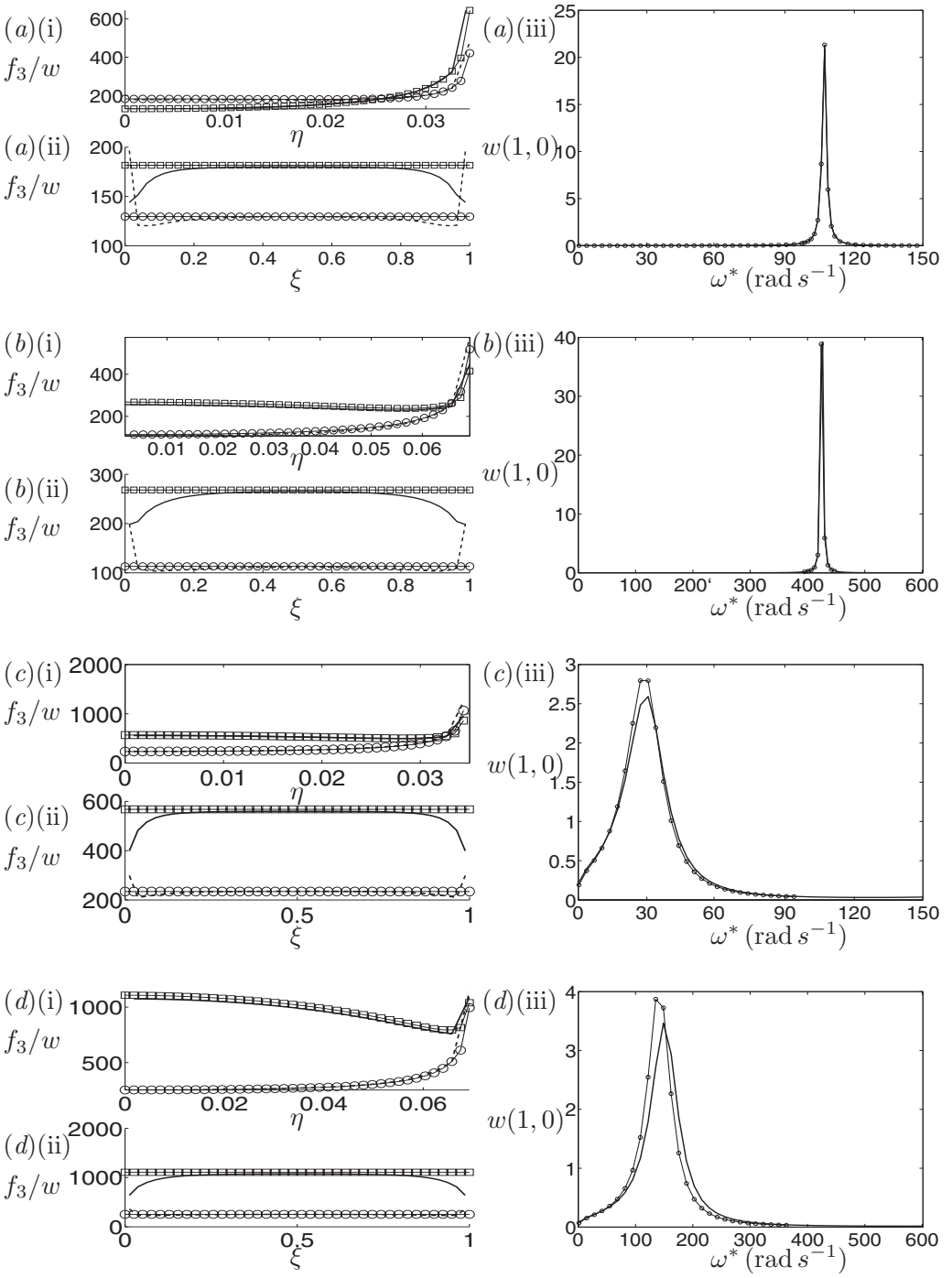

FIG. 9. Thermal responses (iii) of plates C1 (a), (c) and C2 (b), (d) immersed in unbounded (a), (b) air and (c), (d) water, plotted against radial oscillation frequency ω^* and computed using the plate equations subject to 3D TPT (35) (thick solid lines) and 2D BEM hydrodynamic loading (circular markers). Panels (i) and (ii) show profiles of the real (solid lines) and imaginary (dashed lines) of components of 3D TPT loading across ξ=0.5 and η=0, respectively, and similarly for 2D BEM loading (square and circular markers for real and imaginary parts, respectively), at resonance.

simulation, they lie beyond the ambitions of the simple heuristic models presented here (but nonetheless warrant future study in a device-specific context). Nevertheless, in the quest for ever more precise measurements and data interpretation, this study suggests that the choice between two- and three-dimensional hydrodynamic models should be made with some care.

Beyond the microdevice context which directly motivates this study, the thin-plate-theory approximation has the potential to ease the computational burden across a whole range of coupled fluid-structure interaction problems in the low-Reynolds-number regime. Again, the precise details of the flow may be affected to some extent by the particulars of the geometry enclosing the plate; what we present here are the

general trends which we expect for elastic plates operating in a host of different microdevices. The ability of a single distribution of singularities to capture the additive hydrodynamic loading on a thin body, where a nearby boundary produces pronounced differences in the stress profiles on the upper and lower surfaces, is a useful and perhaps surprising feature of the thin-plate-theory approximation.

ACKNOWLEDGMENTS

This work was supported by EPSRC Grant No. GR/R88991 and was performed in collaboration with Prof. Phil Williams in the Laboratory of Biophysics and Surface Analysis, within the School of Pharmacy at The University of Nottingham.

APPENDIX A: THREE-DIMENSIONAL OSCILLATORY STOKESLET ABOVE A WALL

The three-dimensional oscillatory Stokeslet which satisfies no-slip and no-penetration conditions at the plane wall ($x_3=0$) was computed by Pozrikidis [18] and can be expressed in the form

$$\bar{S}_{ij}(\boldsymbol{x},\boldsymbol{X};\gamma,\Delta) = S_{ij}(\hat{\boldsymbol{x}};\gamma) - S_{ij}(\bar{\boldsymbol{x}};\gamma) + \Upsilon_{ij}(\boldsymbol{x},\boldsymbol{X};\gamma,\Delta), \quad i,j=1,2,3, \tag{A1}$$

where $\bar{\boldsymbol{x}}=\boldsymbol{x}^w-\boldsymbol{X}$, $\boldsymbol{x}^w$ is the image of $\boldsymbol{x}$ in the wall, and S_{ij} is the free-space oscillatory Stokeslet

$$S_{ij}(\hat{\boldsymbol{x}};\gamma) = A(\hat{r};\gamma)\frac{\delta_{ij}}{\hat{r}} + B(\hat{r};\gamma)\frac{\hat{x}_i\hat{x}_j}{\hat{r}^3}. \tag{A2a}$$

Here $\hat{r}=|\hat{\boldsymbol{x}}|$ and

$$A(\hat{r};\gamma) = 2e^{-\sqrt{i}\gamma\hat{r}}\left(1+\frac{1}{\sqrt{i}\gamma\hat{r}}-\frac{i}{\gamma^2\hat{r}^2}\right)+\frac{2i}{\gamma^2\hat{r}^2}, \tag{A2b}$$

$$B(\hat{r};\gamma) = -2e^{-\sqrt{i}\gamma\hat{r}}\left(1+\frac{3}{\sqrt{i}\gamma\hat{r}}-\frac{3i}{\gamma^2\hat{r}^2}\right)-\frac{6i}{\gamma^2\hat{r}^2}. \tag{A2c}$$

The wall-interaction tensor Υ_{ij} involves integrals over the wall,

$$2\pi\gamma^4\Upsilon_{i3}(\boldsymbol{x},\boldsymbol{X};\gamma,\Delta) = (\delta_{i3}\partial_k\partial_k - \partial_i\partial_3)\Sigma_1(\boldsymbol{x},\boldsymbol{X};\gamma), \tag{A3a}$$

$$2\pi\gamma^4\Upsilon_{ij}(\boldsymbol{x},\boldsymbol{X};\gamma,\Delta) = \partial_j[\partial_i\Sigma_2(\boldsymbol{x},\boldsymbol{X};\gamma) + (\delta_{i3}\partial_k\partial_k - \partial_i\partial_3)\Sigma_3(\boldsymbol{x},\boldsymbol{X};\gamma)], \tag{A3b}$$

where $\partial_k \equiv \partial/\partial x_k$ for $i,k=1,2,3$ (sum over k) and $j=1,2$ with

$$\Sigma_1(\boldsymbol{x},\boldsymbol{X};\gamma) = \int_0^\infty b(a+b)[(1-e^{(a-b)X_3})e^{-ax_3} + (1-e^{(b-a)X_3})e^{-bx_3}]J_0(b\varrho)db, \tag{A3c}$$

$$\Sigma_2(\boldsymbol{x},\boldsymbol{X};\gamma) = \int_0^\infty a(a+b)(1-e^{(b-a)X_3})e^{-bx_3}J_0(b\varrho)db, \tag{A3d}$$

$$\Sigma_3(\boldsymbol{x},\boldsymbol{X};\gamma) = \int_0^\infty (a+b)(1-e^{(a-b)X_3})e^{-ax_3}J_0(b\varrho)db, \tag{A3e}$$

where $a^2=b^2+i\gamma^2$, $\varrho=\sqrt{\hat{x}_1^2+\hat{x}_2^2}$, and J_0 is a Bessel function of the first kind.

APPENDIX B: TWO-DIMENSIONAL OSCILLATORY STOKESLET ABOVE A WALL

The two-dimensional oscillatory Stokeslet which satisfies no slip and no penetration conditions on the wall $x_3=0$ was computed by Chu and Kim [22] to be

$$\bar{S}'_{ij}(\boldsymbol{x},\boldsymbol{X};\gamma') = S'_{ij}(\hat{\boldsymbol{x}};\gamma') + \Lambda_{ij}(\boldsymbol{x},\boldsymbol{X};\gamma'), \quad i,j=1,2, \tag{B1a}$$

where $\hat{\boldsymbol{x}}=\boldsymbol{x}-\boldsymbol{X}$ and S'_{ij} is the two-dimensional oscillatory free-space Stokeslet [30]

$$S'_{ij}(\hat{\boldsymbol{x}};\gamma') \equiv \frac{2}{i(\gamma')^2}\left(\frac{\delta_{ij}}{\hat{r}^2}-\frac{2\hat{x}_i\hat{x}_j}{\hat{r}^4}\right) - 2K_0(\sqrt{i}\gamma'\hat{r})\left(\delta_{ij}-\frac{\hat{x}_i\hat{x}_j}{\hat{r}^2}\right) - \frac{2K_1(\sqrt{i}\gamma'\hat{r})}{\sqrt{i}\gamma'\hat{r}}\left(\delta_{ij}-\frac{2\hat{x}_i\hat{x}_j}{\hat{r}^2}\right) \tag{B1b}$$

($\hat{r}=|\hat{\boldsymbol{x}}|$) and

$$\Lambda_{ij}(\boldsymbol{x},\boldsymbol{X};\gamma') = (-1)^{\delta_{i1}}\partial_i\Psi_j(\boldsymbol{x},\boldsymbol{X};\gamma'), \tag{B1c}$$

where

$$\Psi_1(\boldsymbol{x},\boldsymbol{X};\gamma') = \frac{1}{2\pi(\sqrt{i}\gamma')^2}\int_0^\infty \frac{1}{q-k}((q+k)(e^{-k(x_3+X_3)} + e^{-q(x_3+X_3)}) - 2qe^{-kx_3-qX_3} - 2ke^{-qx_3-kX_3})\cos kx_2 dk, \tag{B1d}$$

$$\Psi_2(\boldsymbol{x},\boldsymbol{X};\gamma') = \frac{1}{2\pi(\sqrt{i}\gamma')^2}\int_0^\infty \frac{1}{q(q-k)}((q+k)(qe^{-k(x_3+X_3)} + ke^{-q(x_3+X_3)}) - 2kq(e^{-kx_3-qX_3} + e^{-qx_3-kX_3}))\sin kx_2 dk \tag{B1e}$$

($q=\sqrt{k^2+i\gamma'^2}$, $\partial_i=\partial/\partial x_i$) is the wall-interaction term (calculated using Fourier transforms).

[1] G. G. Stokes, Trans. Cambridge Philos. Soc. **9**, 182 (1851).
[2] N. C. Santos and M. A. R. B. Castanho, Biophys. Chem. **107**, 133 (2004).
[3] J. E. Sader, J. Appl. Phys. **84**, 64 (1998).
[4] C. P. Green and J. E. Sader, Phys. Fluids **17**, 073102 (2005).
[5] R. J. Clarke, O. E. Jensen, J. Billingham, A. P. Pearson, and P. M. Williams, Phys. Rev. Lett. **96**, 050801 (2006).
[6] M. R. Paul and M. C. Cross, Phys. Rev. Lett. **92**, 235501 (2004).
[7] N. H. Green, S. Allen, M. C. Davies, C. J. Roberts, S. J. B. Tendler, and P. M. Williams, Trends Analyt. Chem. **21**, 64 (2002).
[8] J. E. Sader and L. R. White, J. Appl. Phys. **74**, 1 (1993).
[9] J. E. Sader, I. Larson, P. Mulvaney, and L. R. White, Rev. Sci. Instrum. **66**, 3789 (1995).
[10] R. W. Stark, T. Drobek, and W. M. Heckl, Ultramicroscopy **86**, 207 (2001).
[11] R. J. Clarke, O. E. Jensen, J. Billingham, and P. M. Williams, Proc. R. Soc. London, Ser. A **462**, 913 (2006).
[12] R. J. Clarke, S. M. Cox, P. M. Williams, and O. E. Jensen, J. Fluid Mech. **545**, 397 (2005).
[13] C. P. Green and J. E. Sader, J. Appl. Phys. **92**, 6262 (2002).
[14] S. Timoshenko and S. Woinowsky-Krieger, *Theory of Shells and Plates* (McGraw-Hill, New York, 1959).
[15] G. K. Batchelor, *An Introduction to Fluid Dynamics* (Cambridge University Press, New York, 1967).
[16] T. Veijola, J. Micromech. Microeng. **14**, 1109 (2004).
[17] M. Loewenberg, J. Fluid Mech. **265**, 265 (1994).
[18] C. Pozrikidis, Phys. Fluids A **1**, 1508 (1989).
[19] W. R. Dean and P. E. Montagnon, Proc. Cambridge Philos. Soc. **45**, 389 (1949).
[20] S. H. Smith, Q. J. Mech. Appl. Math. **48**, 285 (1995).
[21] S. H. Smith, Q. Appl. Math. **55**, 1 (1997).
[22] J. Chu and M-U. Kim, Fluid Dyn. Res. **29**, 7 (2001).
[23] C. Pozrikidis, *Boundary Integral and Singularity Methods for Linearized Viscous Flow* (Cambridge University Press, New York, 1992).
[24] M-U. Kim, K. W. Kim, Y.-H. Cho, and B. M. Kwak, Fluid Dyn. Res. **29**, 171 (2001).
[25] J. W. M. Chon, P. Mulvaney, and J. E. Sader, J. Appl. Phys. **87**, 3978 (2000).
[26] S. Basak, A. Raman, and S. V. Garimella, J. Appl. Phys. **99**, 114906 (2006).
[27] E. O. Tuck, J. Eng. Math. **3**, 29 (1969).
[28] A. Maali, C. Hurth, R. Boisgard, C. Jai, T. Cohen-Bouhacina, and J. P. Aime, J. Appl. Phys. **97**, 074907 (2005).
[29] M. T. Clark and M. R. Paul, J. Appl. Phys. **103**, 094910 (2008).
[30] A. Avudainayagam and J. Geetha, J. Eng. Math. **33**, 251 (1998).